

1 **Tissue environment, not ontogeny, defines murine intestinal**  
2 **intraepithelial T lymphocytes**

3

4 Alejandro J. Brenes<sup>1,3#</sup>, Maud Vandereyken<sup>2#</sup>, Olivia J. James<sup>2</sup>, Harriet Watt<sup>2</sup>, Jens Hukelmann<sup>1§</sup>, Laura  
5 Spinelli<sup>3</sup>, Dina Dikovskaya<sup>2</sup>, Angus I. Lamond<sup>1</sup>, Mahima Swamy<sup>2,3\*</sup>

6

7 <sup>1</sup>Centre for Gene Regulation and Expression, <sup>2</sup>MRC Protein Phosphorylation and Ubiquitylation Unit,

8 <sup>3</sup>Division of Cell Signalling and Immunology, School of Life Sciences, University of Dundee, Dundee DD1  
9 5EH, United Kingdom

10 <sup>§</sup>Present Address: Immatics, Paul-Ehrlich-Str. 15, Tuebingen, 72076, Germany

11 \*Address correspondence to: Dr. Mahima Swamy, Email: [m.swamy@dundee.ac.uk](mailto:m.swamy@dundee.ac.uk)

12 <sup>#</sup>These authors contributed equally

13

14    **Abstract**

15    Tissue-resident intestinal intraepithelial T lymphocytes (T-IEL) patrol the gut and have important roles in  
16    regulating intestinal homeostasis. T-IEL include both induced T-IEL, derived from systemic antigen-  
17    experienced lymphocytes, and natural IEL, which are developmentally targeted to the intestine. While the  
18    processes driving T-IEL development have been elucidated, the precise roles of the different subsets and  
19    the processes driving activation and regulation of these cells remain unclear. To gain functional insights into  
20    these enigmatic cells, we used high-resolution, quantitative mass spectrometry to compare the proteomes of  
21    induced T-IEL and natural T-IEL subsets, with naive CD8<sup>+</sup> T cells from lymph nodes. This data exposes the  
22    dominant effect of the gut environment over ontogeny on T-IEL phenotypes. Analyses of protein copy  
23    numbers of >7000 proteins in T-IEL reveal skewing of the cell surface repertoire towards epithelial  
24    interactions and checkpoint receptors; strong suppression of the metabolic machinery indicating a high  
25    energy barrier to functional activation; upregulated cholesterol and lipid metabolic pathways, leading to high  
26    cholesterol levels in T-IEL; suppression of T cell antigen receptor signalling and expression of the  
27    transcription factor TOX, reminiscent of chronically activated T cells. These novel findings illustrate how T-  
28    IEL integrate multiple tissue-specific signals to maintain their homeostasis and potentially function.

29

30

31

## Introduction

The presence of tissue resident immune cells enables a quick response to either local stress, injury or infection. Understanding the functional identity of immune cells and their shaping by the tissue environment is therefore critical to understanding tissue immunity. Intestinal intraepithelial T lymphocytes (T-IEL) reside within the intestinal epithelium and consist of a heterogeneous mix of natural and induced T-IEL (Olivares-Villagómez and Van Kaer, 2018). All T-IEL express a T cell antigen receptor (TCR), consisting of either  $\alpha\beta$ , or  $\gamma\delta$  chains, alongside TCR co-receptors, i.e., CD8 $\alpha\beta$  or CD8 $\alpha\alpha$  and to a lesser extent CD4(+/-). The most prevalent IEL subsets within the epithelium of the murine small intestine are derived directly from thymus progenitors, so-called natural, or unconventional T-IEL. These natural T-IEL express either TCR $\gamma\delta$  and CD8 $\alpha\alpha$  (TCR $\gamma\delta$  CD8 $\alpha\alpha$  T-IEL), which account for ~50% of the total T-IEL pool, or express TCR $\alpha\beta$  and CD8 $\alpha\alpha$  (TCR $\beta$  CD8 $\alpha\alpha$  T-IEL), which account for ~25% of the total T-IEL. TCR $\beta$  CD8 $\alpha\alpha$  T-IEL are derived from CD4<sup>-</sup>CD8<sup>-</sup> double negative (DN) progenitors in the thymus by agonist selection. Conversely, induced T-IEL are antigen-experienced, conventional CD4<sup>+</sup> or CD8 $\alpha\beta$ <sup>+</sup>  $\alpha\beta$  T cells that are induced to establish tissue-residency within the intestinal epithelium, most likely in response to cues from dietary antigens and the microbiota, as evidenced by a strong reduction in their numbers in germ-free and protein antigen-free mice (Di Marco Barros et al., 2016). These induced T-IEL (TCR $\beta$  CD8 $\alpha\beta$  T-IEL) are believed to have substantial overlap with tissue-resident memory T ( $T_{RM}$ ) cells (Sasson et al., 2020) and are present in high numbers in human intestines. How these induced T-IEL are formed, their functional importance, and the role of the gut environment in deciding their fate are still the focus of intense study.

Residing at the forefront of the intestinal lumen, T-IEL are exposed to a range of commensal bacteria and their metabolites, dietary metabolites and antigens, and potential pathogens. These immune cells are therefore faced with the conflicting tasks of protecting the intestinal barrier, while also preventing indiscriminate tissue damage. Previous gene expression studies have identified T-IEL as having an 'activated-yet-resting' phenotype, with the expression of several activation markers, such as Granzymes and CD44, along with inhibitory receptors, such as the Ly49 family and CD8 $\alpha\alpha$  (Denning et al., 2007; Fahrner et al., 2001; Shires et al., 2001). Yet it is still unclear how T-IEL are kept in check at steady-state (Vandereyken et al., 2020). T-IEL effector responses can get dysregulated in chronic inflammatory conditions, such as celiac disease and inflammatory bowel diseases, therefore we need insight into the regulation of these cells. Moreover, we lack an understanding of how T-IEL are programmed to respond to specific epithelial signals, and how this is dictated and regulated by the tissue microenvironment.

In this study, we use quantitative proteomics to explore the differences between induced T-IEL and systemic T cells from lymph nodes (LN), from which induced T-IEL are ostensibly derived. We also compare induced T-IEL with the natural TCR $\gamma\delta$  and TCR $\alpha\beta$  T-IEL subsets in the gut. Our findings suggest that the tissue environment largely overrides any developmental imprinting of the cells to define the proteomic landscape of intestinal resident T-IEL, and reveal important metabolic and protein translation constraints to T-IEL activation. Importantly, we also uncover evidence of chronic T cell activation potentially driving a partially exhausted phenotype in both the induced and natural T-IEL subsets.

## Results

### Tissue microenvironment defines intestinal T-IEL as distinct from systemic T cells

CD8<sup>+</sup> T-IEL subsets were purified from wild type (WT) murine small intestinal epithelial preparations to greater than 95% purity by cell sorting (**Figure 1—figure supplement 1**). Next, high resolution mass spectrometry (MS) was performed to obtain an in-depth characterisation of the proteomes of the three main CD8<sup>+</sup> T-IEL subsets in the intestine. Tandem mass tags (TMT) were used with synchronous precursor selection (SPS) to obtain the most accurate quantifications for all populations (**Figure 1a**). To evaluate how T-IEL related to other immune populations, we first compared the proteomes of T-IEL with other TMT-based proteomes of various T cell populations currently available within the Immunological Proteome Resource (ImmPRes <http://immpres.co.uk>), an immune cell proteome database developed in-house (Howden et al., 2019). Even though T-IEL are thought to have an effector-like phenotype, by using Principal Component Analysis (PCA), we found that T-IEL were much more similar to *ex-vivo* naïve CD8<sup>+</sup> T cells, than to *in-vitro* activated, effector cytotoxic T cells (CTL) (**Figure 1b**). Hence, we did an in-depth, protein-level comparison of the three T-IEL subsets with two naïve CD8<sup>+</sup> T cells from the lymph nodes (LN). The two LN naïve CD8<sup>+</sup> T cells used here, were either derived from WT mice, similar to the T-IEL, or from P14 transgenic mice, which express a T cell antigen receptor (TCR) specific for a peptide derived from lymphocytic choriomeningitis virus (LCMV). P14 T cells were included as a genetically and developmentally distinct comparator for WT LN T cells. To enable cross-comparisons, all 5 populations were acquired using the same TMT-based SPS-MS3 method and they were all analysed together using MaxQuant (Cox and Mann, 2008). The data were searched using a 1% false discovery rate (FDR) at the protein and peptide spectrum match (PSM) level (for more details see methods). This provided an in-depth overview of the proteome, with over 8,200 proteins detected in total, where each of the 5 populations showed similar coverage, ranging from 6,500 to 7,500 proteins detected in all of them (**Figure 1c**).

For all downstream analyses we converted the raw mass spectrometry intensity values into estimated protein copy numbers using the 'proteomic ruler' (Wisniewski et al., 2014). First, these copy numbers were used to estimate the total protein content for all 5 populations, which revealed no major differences in most, except for the TCR $\gamma\delta$  CD8 $\alpha\alpha$  T-IEL which displayed a slightly higher protein content than the rest (**Figure 1d**). Next, the copy numbers were used as input for a second dimensionality reduction analysis via PCA, focussed now on comparing the T-IEL and LN populations. The results indicated that across the first component, which explains 44% of variance, there was a clear separation between T-IEL and LN populations (**Figure 1e**), highlighting that the 3 T-IEL subsets share much closer identity to each other, than to the naïve LN T cell populations.

To explore these results further we compared each population to each other. As induced TCR $\alpha\beta$  CD8 $\alpha\beta$  T-IEL are thought to be derived from systemic T cells that respond to antigen in organised lymphoid structures, and then migrate into intestinal tissues, we first compared their proteome to the systemic WT LN TCR $\alpha\beta$  CD8 $\alpha\beta$  T cells. Unexpectedly, the Pearson correlation coefficient comparing the estimated protein copy number of TCR $\alpha\beta$  CD8 $\alpha\beta$  T-IEL and the WT LN TCR $\alpha\beta$  CD8 $\alpha\beta$  T cells, was only 0.85, the lowest value in all the comparisons (**Figure 1f**). In contrast, the proteomes of induced T-IEL and the so-called natural T-IEL populations, showed greater similarity with a correlation >0.93 (**Figure 1g,h**), while the correlation between



109 LN T cells from WT to P14 TCR transgenic mice was 0.92 (**Figure 1i**). These analyses indicated that  
110 induced T-IEL share a very similar expression profile to natural T-IEL. The comparisons to LN T cells  
111 revealed that even LN T cells derived from two different strains of mice were much more similar to each  
112 other than to induced T-IEL.

113 To further explore similarities and differences between induced T-IEL and LN T cells we focussed on the  
114 TCRαβ CD8αβ T-IEL and the WT LN TCRαβ CD8αβ T cells (LN). We first performed a global analysis of the  
115 most abundant protein families that represent the top 50% of the proteome. This overview revealed some  
116 similarities and some important proteomic differences between the two cell types. Though the histone  
117 content and the glycolytic enzymes looked very similar, there were big differences in proteins related to the  
118 ribosomes, the cytoskeleton and the cytotoxic granules (**Figure 2a**). The LN population had nearly double  
119 the number of ribosomal proteins, while the T-IEL displayed higher cytoskeletal and cytotoxic proteins.  
120 These proteomic differences were not exclusive to TCRαβ CD8αβ T-IEL, as the same pattern was observed  
121 within both natural T-IEL subsets. Perhaps the most striking difference between naïve LN T cells and T-IEL  
122 was the expression levels of Granzymes (**Figure 2b**). Granzyme A (GzmA) was expressed at >20 million  
123 copies per cell in each of the natural T-IEL subsets, and at 9-10 million molecules per cell in the induced T-  
124 IEL population. This was more than double what was previously identified in cytotoxic CD8<sup>+</sup> T cells (Howden  
125 et al., 2019). Granzyme B (GzmB), which was expressed at ~20 million copies per cell in CTL, was  
126 expressed at between 4 to 10 million copies per cell in all 3 T-IEL subsets. T-IEL also express Granzyme C  
127 (GzmC) and K (GzmK), although at <100,000 molecules per cell each (**Figure 2b**), making their general  
128 expression of Granzymes either comparable to, or higher than, *in vitro*-generated CTL. This substantial  
129 commitment to Granzyme expression is consistent with the expression of the whole cytotoxic machinery,  
130 including perforin and key molecules involved in degranulation (**Supplementary File 1**, (James et al.,  
131 2020)), all of which are either barely detectable, or altogether absent, in the naïve T cells. Thus, these data  
132 support the hypothesis that all T-IEL in the gut are geared towards cytotoxic activity.

133 To obtain an unbiased overview of the differences between the induced T-IEL and the LN T cell populations,  
134 we performed an overrepresentation analysis (ORA) focussed on Gene Ontology (GO) terms related to  
135 biological processes (**Figure 2c-d; Supplementary Files 2,3**). The data indicated that proteins which were  
136 significantly increased in expression in induced T-IEL were highly enriched in cholesterol and lipid  
137 metabolism, intestinal absorption and xenobiotic metabolism and processes involving cytoskeletal proteins,  
138 such as cell-cell adhesion and integrin-mediated signalling. Conversely, proteins which were significantly  
139 higher expressed in LN T cells were enriched for terms relating to ribosomal proteins and ribonuclease P  
140 activity.

141

## 142 **Downregulation of protein synthesis in T-IEL**

143 Based on the results obtained from the ORA, we next focussed on the protein machinery involved with the  
144 ribosomes and protein synthesis. A comparison of the total estimated copy numbers for ribosomal proteins  
145 indicated that LN T cells express almost double the amount expressed in any of the T-IEL subsets (**Figure**  
146 **3a**). This was true for both cytoplasmic and mitochondrial ribosomal proteins, with the latter being the most

147 reduced in T-IEL, compared to LN T cells. The decreased expression of ribosomal proteins in T-IEL was  
148 mirrored by the decreased expression of RNA polymerases I (Pol1) and III (Pol3), which transcribe,  
149 respectively, ribosomal RNA and transfer RNA (**Figure 3b**). For the subunits of both the Pol1 and Pol3  
150 complexes, the median fold reduction in T-IEL was greater than 5-fold when compared to LN T cells (**Figure**  
151 **3- figure supplement 1**). Strikingly, the subunits specific for RNA polymerase II (Pol2), which transcribes  
152 protein-coding genes, did not display a reduction in median expression levels. These data suggest that while  
153 ribosomal expression is reduced, mRNA pools could potentially still be maintained in T-IEL.

154 To maintain protein synthesis, consistent uptake of amino acids is generally required. However, our data  
155 show that T-IEL express low levels (<2000 copies per cell) of 3 key amino acid transporters, i.e., SLC1A5,  
156 SLC7A5 and SLC38A2 (**Figure 3c**), all of which are highly upregulated upon T cell activation with SLC7A5  
157 being expressed at >400,000 copies in effector T cells (Howden et al., 2019). SLC7A5 expression levels  
158 have been reported to directly control the expression of ribosomal proteins and other important translation  
159 machinery components (Marchingo et al., 2020; Sinclair et al., 2019). The very low levels of amino acid  
160 transporters detected in T-IEL is therefore expected to limit protein synthesis. Furthermore, despite having  
161 low levels of amino acid transporters, enzymes involved in amino acid catabolism, such as arginase-2  
162 (ARG2) and alanine aminotransferase (Glutamic-Pyruvic Transaminase, GPT), are highly expressed in T-  
163 IEL, also suggesting reduced protein synthesis in T-IEL (**Figure 3d**). Interestingly, high expression of ARG2  
164 was also accompanied by upregulated expression of other enzymes from the urea cycle (**Figure 3- figure**  
165 **supplement 1**). Finally, it is also notable that T-IEL express significantly higher levels of PRKR-Like  
166 Endoplasmic Reticulum Kinase (PERK), than LN T cells. PERK functions as a global protein synthesis  
167 inhibitor, either in the presence of unfolded proteins, or upon low amino acid availability (**Figure 3e**). We  
168 therefore decided to measure the protein synthesis rates in T-IEL and LN T cells by O-propargyl puromycin  
169 (OPP) incorporation into nascent peptide chains and compared with cycloheximide-treated controls. The  
170 data from the OPP assay highlighted almost undetectable levels of protein translation in all 3 T-IEL subsets  
171 (**Figure 3f**), which correlated well with the reduced ribosomal content, low expression of amino-acid  
172 transporters and high catabolic enzymes identified within the proteomes of T-IEL. In contrast, LN T cells  
173 contain more actively translating ribosomes than T-IEL, providing orthogonal validation of the proteomic  
174 data. It should be noted that naïve T cells have been reported to have low protein synthesis rates (Wolf et  
175 al., 2020), however, our data indicate even lower synthesis rates in T-IEL. Thus, multiple mechanisms  
176 appear to be active in T-IEL to keep protein synthesis at a minimum.

### 177 **T-IEL have a unique metabolic profile**

178 Recent studies have shown a direct correlation between metabolic activity and the rates of protein synthesis  
179 in T cells (Argüello et al., 2020). The very low levels of protein synthesis in all 3 T-IEL subsets therefore  
180 prompted us to further explore the bioenergetic profile of T-IEL. Globally, we did not find any major  
181 differences in the proportion of the T-IEL proteomes dedicated to the major metabolic pathways compared to  
182 naïve T cells (**Figure 4a**). We did however find that all 3 T-IEL subsets express substantial levels of the  
183 GLUT2 (~5,000 copies) and GLUT3 (~35,000 copies), both facilitative glucose transporters (**Figure 4b**).  
184 GLUT2 is normally found in intestinal and other epithelial cells, not in immune cells, and is a low affinity  
185 bidirectional glucose transporter. GLUT3 is a high affinity glucose transporter that is thought to be particularly

186 important in CD8 T cell activation (Geltink et al., 2018). Glucose can be utilised in T cells through either  
187 glycolysis, or oxidative phosphorylation (OXPHOS) and the tricarboxylic acid (TCA) cycle that also provides  
188 biosynthetic intermediates (Ma et al., 2019). We therefore examined the expression of proteins involved in  
189 these pathways in T-IEL. We find that T-IEL express most of the proteins of the glycolytic and TCA pathways  
190 at similar levels to naïve T cells (**Figure 4c**). With one exception being the lactate transporters, SLC16A1  
191 and SLC16A3, which even though they are significantly higher than in naïve T cells, are still expressed at  
192 very low levels, indicating a low glycolytic potential within these cells. Furthermore, T-IEL have also been  
193 shown to have comparably low OXPHOS potential as in naïve T cells (Konjar et al., 2018). Thus, the function  
194 of the glucose being taken up through the T-IEL glucose transporters remains unclear.

195 We also examined the mitochondrial protein content of T-IEL. The total mitochondrial protein content  
196 appeared to be significantly reduced, however, all the components of the electron transport chain (ETC)  
197 were expressed at similar levels in all T-IEL, as in LN T cells (**Figure 4d**). These data suggest that T-IEL  
198 mitochondria have similar respiratory capacity to naïve T cells. Naïve T cells use OXPHOS and fatty acid  
199 oxidation (FAO) to maintain their cellular functions. Therefore, we assessed FAO enzyme expression in T-  
200 IEL, and found this was also largely similar to naïve T cells (**Figure 4c**). Interestingly, some proteins  
201 involved in peroxisomal FAO, including the transporter ABCD4, the key peroxisomal beta-oxidation enzymes  
202 acyl-CoA oxidase ACOX1, and Carnitine O-Acetyltransferase (CrAT), were more highly expressed in T-IEL  
203 than in naïve T cells. Peroxisomal FAO produces Acetyl CoA, which can be used within the TCA cycle, and  
204 NADH, which can be utilised in the ETC, to contribute to energy production. NADH produced during FAO  
205 and OXPHOS needs to be transported into the mitochondria through a redox shuttle, and in this context, we  
206 find that the glycerol-3-phosphate shuttle is only expressed in T-IEL (**Figure 4e**). Put together, these data  
207 suggest that peroxisomes may be a source of fuel to support the low levels of energy produced in T-IEL, and  
208 indicate key differences in the metabolic pathways active in T-IEL.

## 209 **T-IEL have increased lipid biosynthesis and cholesterol metabolism**

210 Our data would seem to indicate that T-IEL have low bioenergetic production and requirements. However,  
211 functional annotation of proteins enriched in induced T-IEL indicate over-representation of cholesterol and  
212 steroid metabolism pathways, and the metabolism of chemicals and inorganic compounds (**Figure 2c**). T-IEL  
213 are highly enriched in proteins involved in xenobiotic metabolism, including members of the UDP  
214 glucuronosyl transferase (UGT) family, Glutathione S-transferase (GST) and Cytochrome P450 (CYP)  
215 enzymes (**Supplementary File 1**). Detailed examination of the cholesterol biosynthetic pathway indicates  
216 almost all the enzymes are expressed highly in all T-IEL, as compared to LN T cells (**Figure 5a**). This  
217 pathway is controlled by the master regulator sterol-regulatory element binding protein 2 (SREBP2)  
218 (Madison, 2016), which the data show is exclusively expressed within the 3 T-IEL populations (**Figure 5b**).  
219 We therefore measured cholesterol content in T-IEL, and found that indeed all 3 subsets have greater than  
220 2.5-fold more cholesterol than naïve LN CD8 T cells (**Figure 5c**).

221 T-IEL also express the fatty acid transport proteins (FATP2(*Slc27a2*) and FATP4 (*Slc27a4*)), which are  
222 necessary for uptake and transport of long chain fatty acids, as well as fatty acid binding proteins (FABP1, 2,  
223 5 and 6), which also contribute to uptake and transport of fatty acids to the endoplasmic reticulum (ER)  
224 (**Figure 5d,e**). In addition to the intestinal specific family member, FABP2 (>350,000 copies/cell), the liver

225 FABP, FABP1 (>200,000 copies/cell), which is highly expressed in the proximal intestine, and the ileal  
 226 FABP, FABP6 or Gastrotropin (>10,000 copies/cell), are all also highly expressed in all 3 T-IEL subsets  
 227 (**Figure 5e**). It is interesting to note that FABP5, which was previously identified as being expressed in skin  
 228 T<sub>RM</sub> cells, but not in intestinal T<sub>RM</sub> at the mRNA level (Frizzell et al., 2020), was detected at >200,000  
 229 molecules per cell in all 3 T-IEL. Skin T<sub>RM</sub> appear to use increased exogenous fatty acids uptake to feed into  
 230 mitochondrial FAO, thus supporting their maintenance and survival (Pan et al., 2017). However, carnitine O-  
 231 palmitoyl transferase (CPT1A), the rate-limiting enzyme for mitochondrial FAO of long chain fatty acids is  
 232 expressed at lower levels in T-IEL compared to naive LN T cells (**Figure 4c**). This suggests that the highly  
 233 increased lipid transporter expression in T-IEL is not solely used to drive FAO.

234 T-IEL are also enriched in proteins involved in the two major pathways of triacylglycerol (TAG or triglyceride)  
 235 synthesis expressed in the intestine (**Figure 5f**) (Yen et al., 2015). TAG is hydrophobic and is either stored  
 236 transiently in the cytosol in lipid droplets or assembled and secreted from enterocytes in apolipoprotein B  
 237 (ApoB)-containing chylomicrons, or lipoproteins that also contain cholesterol and cholesteryl esters.  
 238 Surprisingly, T-IEL also express high levels of a key cholesterol esterification enzyme, Acyl CoA:cholesterol  
 239 acyl transferase 2, ACAT-2 (*Soat2*), which is thought to be specifically expressed in enterocytes (Pan and  
 240 Hussain, 2012). Esterification of cholesterol increases its hydrophobicity for efficient packaging into  
 241 lipoproteins. We therefore also explored the expression of enzymes involved in lipoprotein assembly.  
 242 Lipoprotein assembly involves the packaging of TAG and cholesteryl esters by the microsomal triglyceride  
 243 transfer protein (MTP, *Mttp*) into ApoB-lipid conjugates, followed by export out of the cells by the core protein  
 244 complex II (COPII) (Hussain et al., 2012). MTP was highly expressed in T-IEL with over 80,000 copies per  
 245 cell, while less than 100 copies were identified in LN T cells. Similarly, ApoB and the GTPase SAR1b, a key  
 246 component of the COPII complex, were also expressed in T-IEL at higher copies than in LN T cells (**Figure**  
 247 **5f**). Together, these data suggest that T-IEL also take up and metabolise fatty acids and cholesterol, and  
 248 further, have the capacity to package these lipids into lipid droplets and potentially even transport them out of  
 249 the cells.

## 250 **Intestinal T-IEL proteome contains cell surface receptors for epithelial and neuroimmune interactions**

251 We also explored the expression of proteins uniquely identified in T-IEL and found several proteins involved  
 252 in cell adhesion, cytoskeleton remodelling and integrin signalling. Strikingly, all T-IEL subsets expressed  
 253 numerous epithelial cell adhesion molecules and integrins which are not found on naïve LN T cells (**Figure**  
 254 **6a**). Although these results are consistent with the localisation of T-IEL within the gut epithelial layer, we  
 255 were surprised to find T-IEL proteomes also contained many tight junction, adherens junction and  
 256 desmosome-associated proteins, which are normally expressed on intestinal epithelial cells, such as E-  
 257 Cadherin (E-Cad), ZO-2, desmoplakin, Villin-1 and JAM-A (F11R) (**Figure 6a,b**). These proteins could  
 258 potentially be contaminants from epithelial cells in the sample preparation, however, E-Cad, Occludin and  
 259 EpCAM have been detected both at the RNA and protein level in T-IEL (**Figure 6- figure supplement 1**,  
 260 (Inagaki-Ohara et al., 2005; Nochi et al., 2004)). Moreover, immunofluorescence imaging and flow cytometry  
 261 confirmed expression of ZO-2, E-Cad and EpCAM in T-IEL, suggesting that T-IEL could use these molecules  
 262 to navigate the tissue environment (**Figure 6c, Figure 6- figure supplement 1**). Conversely, endothelial cell  
 263 adhesion molecules such as PECAM-1 and L-selectin, that facilitate T cell migration into secondary lymphoid

264 organs, were highly expressed on naïve T cells, but not on T-IEL, as befits their tissue resident status  
265 (**Figure 6d**).

266 T-IEL proteomes also suggest that T-IEL could be communicating with the enteric nervous system. TCR $\gamma\delta$   
267 CD8 $\alpha\alpha$  T-IEL express two neural cell adhesion molecules, NCAM1 (CD171) and NrCAM, both implicated in  
268 homophilic adhesion and in axonal growth and guidance. Furthermore, two neuropeptide receptors, GPR171  
269 and VIPR2, were also identified in T-IEL proteomes (**Figure 6b**). BigLEN and vasoactive intestinal peptide  
270 (VIP) bind to GPR171 and VIPR1/VIPR2, respectively (Delgado et al., 2004; Gomes et al., 2013). BigLEN  
271 and VIP are neuropeptides with multiple physiological effects, including gut motility, nutrient absorption, food  
272 intake regulation and immune responses (Yoo and Mazmanian, 2017). VIPR2 expression on intestinal innate  
273 lymphoid cells was shown to regulate their immune response (Seillet et al., 2020; Talbot et al., 2020). In  
274 addition, we also found that T-IEL express GLP1R and GLP2R (**Figure 6b**), receptors for the glucagon-like  
275 peptides 1 and 2 (GLP1 and GLP2), which are intestinal peptides involved in regulating appetite and satiety.  
276 Both of these receptors were previously mainly found on enteroendocrine cells and enteric neurons.  
277 However, recently GLP1R expression on T-IEL was shown to contribute to metabolic syndrome development  
278 in mice (He et al., 2019; Yusta et al., 2015). Together, these data suggest that T-IEL may be involved in  
279 regulating immune responses and potentially also metabolic responses to food intake through their  
280 communication with epithelial cells.

#### 281 **T-IEL share a common signature with exhausted T cells**

282 T-IEL also express many signalling receptors that are absent on naïve T cells and that potentially regulate  
283 their poised activated state (Vandereyken et al., 2020). The proteomic analyses here confirmed that all 3 T-  
284 IEL subsets express many inhibitory receptors, including LAG-3, CD200R1, CD244 and NK receptors, such  
285 as members of the Ly49 family, but also showed that a wider range of these inhibitory receptors are found on  
286 innate T-IEL compared to induced T-IEL (**Figure 6b**). Furthermore, T-IEL, regardless of ontogeny, uniformly  
287 expressed CD38 and CD73 (*Nt5e*) (**Figures 6b,d**). Indeed, co-expression of CD38 and CD73 is seen to  
288 provide a better marker for identifying T-IEL than CD103 expression (**Figure 7a,b**). These receptors are  
289 tightly linked to purinergic signalling through their regulation of P2RX7, and as previously found on T<sub>RM</sub> cells  
290 (Borges da Silva et al., 2018; Stark et al., 2018), P2RX7 and CD39 are also highly expressed on T-IEL,  
291 although less uniformly than CD38 and CD73 (**Figure 7a,b**).

292 CD38 and CD39 have recently been identified as markers of T cell exhaustion, along with expression of PD-  
293 1, LAG-3, CD244, CD160 among other inhibitory receptors. As all these molecules are highly expressed on  
294 T-IEL (**Figure 7a-d**), with the exception of PD-1, T-IEL appear to share some similarities with exhausted T  
295 cells (Alfei et al., 2019; Khan et al., 2019; Scott et al., 2019). An overrepresentation analysis using a  
296 database of T cell exhaustion markers confirmed that T IEL are enriched in markers of exhaustion (**Figure**  
297 **7e**), with at least 76 proteins that were upregulated in exhausted T cells also being upregulated in T-IEL  
298 (**Figure 7f**, top and **Supplementary File 5**). During exhaustion of systemic T cells, several proteins are  
299 downregulated. Interestingly, a significant proportion of these downregulated proteins are also  
300 downregulated in induced T-IEL (**Figure 7f**, bottom and **Supplementary File 5**). We therefore further  
301 examined the expression of transcription factors associated with T cell exhaustion (**Figure 7g**). Indeed, two  
302 transcription factors recently identified to be key to imprinting the 'exhausted' T cell phenotype, i.e., TOX and

NR4A2, were preferentially expressed in all T-IEL, whereas other transcription factors that show reduced expression in exhausted T cells, including TCF1 and LEF1, were also downregulated in T-IEL. We further confirmed expression of TOX in all T-IEL subsets by flow cytometry (**Figure 7h**). However, T-IEL still express high levels of T-bet, as do effector T cells, which most likely helps to maintain expression of cytolytic effector molecules, such as granzymes, while repressing PD-1 expression on T-IEL. Overall, both natural and induced T-IEL appear to have a hybrid phenotype combining features of exhausted T cells and effector T cells, while also bearing unique hallmarks imprinted by the intestinal microenvironment.

#### **Modifications in the T cell antigen receptor signalosome in T-IEL**

Given the connection between T-IEL and exhausted T cells, one key question we wanted to address was whether T-IEL are also unresponsive to TCR stimulation. Indeed, we find that only a small percentage (<10%) of both natural T-IEL subsets are able to respond to TCR crosslinking as measured by induction of phosphorylation of ERK1/2 and S6 ribosomal protein (**Figure 8a,b**). However, induced TCR $\alpha\beta$  CD8 $\alpha\beta$  T-IEL responded even better than LN T cells to TCR stimulation. It has previously been recognised that cross-linking of the TCR on TCR $\gamma\delta$  T-IEL does not induce calcium flux and downstream signalling (Malinarich et al., 2010; Wencker et al., 2014). This reduced TCR signalling capacity has been attributed to chronic TCR signalling in the tissue. However, how TCR signalling is dampened at a mechanistic level has not yet been addressed. We sought to evaluate whether there were changes in the TCR signalosome in T-IEL that were blocking TCR signals, and how conserved it was across the different subsets (**Figure 8c**). Strikingly, several proteins were differentially expressed, not just in TCR $\gamma\delta$  T-IEL, but in all T-IEL subsets including induced TCR $\alpha\beta$  CD8 $\alpha\beta$  T-IEL. Quantitative analysis of the immediate TCR signalling elements confirmed previous studies showing exclusive expression of Fc $\epsilon$ R1 $\gamma$  and LAT2 (NTAL/LAB) on T-IEL, and downregulation of LAT and CD3 $\zeta$  as compared to LN T cells (**Figure 8c**). Replacement of the CD3 $\zeta$  chain with the Fc $\epsilon$ R1 $\gamma$  chain reduces the number of immunoreceptor tyrosine-based activation motifs (ITAMs) in the TCR. LAT2 is reported to play a dominant negative role in TCR signalling by competing with LAT for binding partners, but is unable to couple to PLC $\gamma$  (Fuller et al., 2011).

In addition to LAT and CD3 $\zeta$ , several other proteins were differentially expressed (**Figure 8c,d**). Surprisingly, many proteins normally found in B cells and involved in BCR signal transduction, were identified as expressed in T-IEL, e.g., Lyn, Syk, LAT2, PLC $\gamma$ 2, Themis2, and many of these are also often found in exhausted T cells (**Supplementary File 5**, (Khan et al., 2019; Schietinger et al., 2016)). We also noted the expression of several negative regulators of TCR signalling, including STS-1 (Ubash3b) that dephosphorylates Zap70/Syk, CD148 (PTPRJ) and DUSP6, which negatively regulates MAPK signalling (Gaud et al., 2018) (**Figure 8c,d**). These negative regulators of signalling are also highly expressed in tumour-associated exhausted T cells (Schietinger et al., 2016). Conversely, key TCR signalling intermediates, such as Protein kinase C  $\theta$  (PKC $\theta$ ) and Rac were very poorly expressed. Importantly, many of these changes were not confined to the natural CD8 $\alpha\alpha$  T-IEL subsets but were also identified in induced T-IEL.

In summary, these data suggest that the rewiring of the TCR signalosome in T-IEL occurs independently of the developmental pathway through which the 3 different subsets are derived, and is instead shaped by the intestinal environment. However, as induced T-IEL also express LAT2 and Fc $\epsilon$ R1 $\gamma$  chain, but still respond to

342 TCR signals, the loss of TCR responsiveness in natural T-IEL cannot be solely attributed to these proteins.  
343 Further evaluation of the TCR signalling pathways is necessary to provide an explanation for the loss of TCR  
344 responses in natural T-IEL.

## 345 Discussion

346 Both TCR $\gamma\delta$  and TCR $\alpha\beta$  CD8 $\alpha\alpha$  natural T-IEL have long been considered unconventional T cells, due to  
347 their unique developmental pathways and their strict restriction to the intestinal epithelium. In contrast,  
348 induced T-IEL that arise from systemic antigen-experienced T cells, are considered conventional and more  
349 like memory T cells in their ability to respond rapidly to activation signals. Yet our unbiased analyses clearly  
350 show that induced T-IEL share far greater similarity to other intestinal T cell subsets than to the systemic T  
351 cells they arise from. The T-IEL signature most strikingly contains several proteins thought to be exclusively,  
352 or very highly, expressed by enterocytes. These include cognate proteins involved in mediating adherens  
353 and tight junction formation, showing that T-IEL are strongly integrated into the intestinal epithelium, by  
354 interactions that extend well beyond the CD103: E-cadherin interaction. T-IEL also share metabolic  
355 similarities with enterocytes including a strong enrichment in proteins required for cholesterol, lipid and  
356 xenobiotic metabolism. Many of these genes are aryl hydrocarbon receptor (AHR) targets (Stockinger et al.,  
357 2014; Tanos et al., 2012), suggesting that one reason why AHR is essential for T-IEL survival (Li et al.,  
358 2011) is to protect them from toxins and bacterial metabolites in the gut. Other potential indicators of tissue  
359 adaptation include expression of the intestine-specific GLUT2 glucose transporter, and the high expression  
360 of the urea cycle that could be important for detoxifying the large quantities of ammonia that is present in the  
361 intestinal lumen (Romero-Gomez et al., 2009). Furthermore, we find that despite having very low energy  
362 requirements, T-IEL have a distinct metabolic signature, with high expression of proteins such as GLUT3,  
363 glycerol-3-phosphate shuttle and peroxisomal FAO enzymes. Interestingly, the glycerol phosphate shuttle is  
364 normally only expressed in highly glycolytic cells to maintain cellular redox balance by recycling NAD in the  
365 cytosol, with most other mammalian cells using the malate-aspartate shuttle for this purpose (Mráček et al.,  
366 2013, p.; Spinelli and Haigis, 2018). Thus, we find that T-IEL, far from being metabolically quiescent, have  
367 instead a metabolism tailored to their environment, to protect T-IEL from the harsh intestinal environment  
368 and actively limit proliferation and activation of these cells.

369 Ribosomal content was the one area where T-IEL seemed truly deficient in comparison to naïve LN T cells.  
370 This was surprising, since naïve T cells, like T-IEL, are not actively cycling cells. However, it was recently  
371 shown that a subset of proteins in naïve T cells have short half-lives and are rapidly turned over (Wolf et al.,  
372 2020). These included transcription factors that maintain the naïve state, but that need to be rapidly  
373 degraded upon T cell activation, allowing T cells to differentiate. Naïve T cells were also found to express a  
374 large number of idling ribosomes ready to translate mRNAs required for T cell activation. Thus, the non-  
375 existent ribosomal activity in T-IEL subsets is possibly a reflection of their terminally differentiated status. It is  
376 also interesting to note that amino acid transporters were expressed at very low levels in T-IEL, thus limiting  
377 amino acid availability for protein translation. In this context, we recently showed that activation of T-IEL with  
378 IL-15 involves both upregulation of ribosome biogenesis and upregulation of amino acid transporters (James  
379 et al., 2020). The low rates of protein translation also highlight the importance of studying the proteome in T-  
380 IEL as there may be a significant disconnect between protein and mRNA expression.

381 In identifying proteins that were expressed solely in T-IEL, but not LN T cells, we uncovered a clear signature  
382 of T cell exhaustion within the proteome. Like exhausted T cells, T-IEL have diminished capacity to  
383 proliferate in response to TCR triggering, and increased expression of co-inhibitory molecules. However,  
384 unlike exhausted T cells, T-IEL maintain high levels of cytotoxic effector molecules, suggesting that they are  
385 still capable of killing, although it is unclear what signals are required to trigger full degranulation in T-IEL.  
386 Interestingly, despite identifying more than 30 cell surface proteins on T-IEL that were not expressed in LN T  
387 cells, no one marker was exclusive to T-IEL, as they were either proteins that were normally expressed in  
388 intestinal epithelial cells, or those expressed on activated or exhausted T cells. Thus, the proteomic profiles  
389 of T-IEL reveal an interesting mixture of various T cell types; naïve, effector and exhausted, as well their  
390 unique tissue-specific signatures.

391 T-IEL also display several hallmarks of exhausted or suppressed T cells, including a major rewiring of the  
392 TCR signalosome. We were surprised to find that LAT2, and many negative regulators of signalling, such as  
393 DUSP6 were also expressed in induced T-IEL. These data suggest that the changes in the TCR  
394 signalosome are induced by the gut environment, rather than being developmentally regulated. In addition,  
395 we found that all T-IEL express ACAT2, a key protein involved in cholesterol esterification, that potentially  
396 sequesters cholesterol away from the plasma membrane. Previously, ACAT1, but not the closely related  
397 ACAT2, was found to be upregulated in activated CD8<sup>+</sup> T cells (Yang et al., 2016). Genetic ablation of  
398 ACAT1 lead to increased response from activated T cells in both infection and in cancer, and this was  
399 attributed to the increased cholesterol in the plasma membrane leading to increased TCR clustering (Molnár  
400 et al., 2012; Yang et al., 2016). Indeed, increased cholesterol content has also been shown to potentiate γδ  
401 T cell activation (Cheng et al., 2013). It would be interesting to see if the high levels of ACAT2 expressed in  
402 T-IEL prevent accumulation of cholesterol in the T-IEL membranes, thus increasing the activation threshold  
403 of T-IEL. On a similar note, ARG2, which was highly expressed in T-IEL, has also been shown to block T cell  
404 activation (Geiger et al., 2016; Martí i Líndez et al., 2019), and expression of the alanine metabolizing  
405 enzyme, GPT1, may limit alanine availability for protein synthesis in T cell activation (Ron-Harel et al., 2019).  
406 Thus, multiple lines of evidence support the notion that both natural and induced T-IEL are tightly regulated  
407 through inhibition of signalling.

408 In summary, we have presented an in-depth proteomic analyses and comparisons of induced and natural T-  
409 IEL and systemic T cells. These data provide key insights into the nature of T-IEL as well as the  
410 underappreciated similarities between both induced and natural T-IEL. New findings related to cholesterol  
411 metabolism, a high energy and translation barrier to activation, and transcription factors that potentially  
412 regulate T-IEL function, suggest new ways to investigate how the different T-IEL subsets contribute to tissue  
413 and organismal homeostasis.

#### 414 **Acknowledgements**

415 The authors would like to thank Doreen Cantrell for her critical reading of the manuscript, support and  
416 advice. We also acknowledge the support provided by A. Whigham and R. Clarke from the Flow Cytometry  
417 Facility for cell sorting and flow cytometry, and by the Biological Resources Unit at the University of Dundee.  
418 The contribution of the UK Research Partnership Infrastructure Fund award to the Centre for Translational  
419 and Interdisciplinary Research for the purchase of the mass spectrometers is gratefully acknowledged.



420     **Competing interests**

421     The authors declare that they have no conflict of interest.

422

<b>Key Resources Table</b>				
<b>Reagent type (species) or resource</b>	<b>Designation</b>	<b>Source or reference</b>	<b>Identifiers</b>	<b>Additional information</b>
Genetic reagent (M. musculus)	P14	PMID: 2573841		
Strain, strain background (M. musculus)	C57BL/6J	Charles Rivers	RRID: IMSR_JAX:000664	
Chemical compound, drug	DAPI	Thermo Fisher Scientific	Cat # D1306	1 ug/ml
Antibody	Anti-CD4 (rat, monoclonal)	Thermo Fisher Scientific (eBiosciences)	RRID: AB_494000	cell surface staining (1:200)
Antibody	Anti-CD8a (rat, monoclonal)	Biolegend	RRID: AB_2562558	cell surface staining (1:400)
Antibody	Anti-CD8a (rat, monoclonal)	Biolegend	RRID: AB_312746	immunofluorescence (1:100)
Antibody	Anti-CD8b (rat, monoclonal)	eBioscience	RRID: AB_657764 RRID: AB_1121888	cell surface staining (1:400)
Antibody	Anti-CD38 (rat, monoclonal)	BioLegend	RRID: AB_312928 RRID: AB_312929	Cell surface staining (1:200)
Antibody	Anti-CD39 (rat, monoclonal)	BioLegend	RRID: AB_2563395	Cell surface staining (1:200)
Antibody	Anti-CD44 (rat, monoclonal)	BD Biosciences	RRID: AB_1272244	Cell surface staining (1:200)
Antibody	Anti-CD62L (rat, monoclonal)	Thermo Fisher Scientific	RRID: AB_469632	Cell surface staining (1:200)

Antibody	Anti-CD73 (rat, monoclonal)	BioLegend	RRID: AB_11219608	Cell surface staining (1:200)
Antibody	Anti-CD96 (rat, monoclonal)	BioLegend	RRID: AB_1279389	Cell surface staining (1:200)
Antibody	Anti-CD103 (armenian hamster, monoclonal)	Biolegend	RRID: AB_2563691	Cell surface staining (1:200)
Antibody	Anti-CD160 (rat, monoclonal)	BioLegend	RRID: AB_10960740 RRID: AB_10960743	Cell surface staining (1:200)
Antibody	Anti-CD244 (rat, monoclonal)	eBioscience	RRID: AB_657872	Cell surface staining (1:200)
Antibody	Anti-E-cadherin (mouse monoclonal)	BD Biosciences	RRID: AB_397581	Immunofluorescence (1:100)
Antibody	Anti-LAG-3 (rat, monoclonal)	eBioscience	RRID: AB_2573427	Cell surface staining (1:100)
Antibody	Anti-P2X7R (rat, monoclonal)	BioLegend	RRID: AB_2650951	Cell surface staining (1:200)
Antibody	Anti-TCRb (armenian hamster, monoclonal)	BioLegend	RRID: AB_2629696	Cell surface staining (1:100)
Antibody	Anti-EpCam (rat, monoclonal)	eBioscience	RRID: AB_953617	Cell surface staining (1:200)
Antibody	Anti-E-Cadherin (rat, monoclonal)	eBioscience	RRID: AB_1834417	Cell surface staining (1:100)
Antibody	Anti- TCR $\gamma\delta$ (armenian hamster, monoclonal)	BioLegend	RRID: AB_2563356	Cell surface staining (1:200)

Antibody	Anti-phospho S6 (S235/236) (rabbit, monoclonal)	Cell Signaling Technology	RRID: AB_916156	Intracellular staining (1:25)
Antibody	Anti-phospho ERK1/2 (T202/Y204) (rabbit, monoclonal)	Cell Signalling Technology	RRID: AB_331775	Intracellular staining (1:200)
Antibody	Anti-ZO-2 (rabbit polyclonal)	Cell Signaling Technology	RRID: AB_2203575	Immunofluorescence (1:50)
Antibody	Anti-CD3e (armerian hamster, monoclonal)	BioLegend	RRID: AB_312667	TCR stimulation (30ug/ml)
Chemical compound, drug	PP2	Merck (Calbiochem)	Cat # 529573	TCR stimulation, Src inhibitor
Chemical compound , drug	O-Propargyl-puromycin	JenaBioscience	NU-931-05	Protein synthesis measurements
Commercial assay or kit	EasySep CD8+ T cell isolation kit	STEMCELL Technologies, UK	Cat # 19853	For isolating CD8+ T cells from LNs
Commercial assay or kit	EasySep Mouse CD8a Positive Selection Kit II	STEMCELL Technologies, UK	Cat # 18953	For enriching CD8a+ IEL
Commercial assay or kit	EasySep Dead Cell Removal (Annexin V) Kit	STEMCELL Technologies, UK	Cat # 17899	For removing dead epithelial cells and enriching IEL
Commercial assay or kit	Amplex Red cholesterol Assay Kit	Invitrogen	Cat # A12216	Cholesterol assay
Commercial assay or kit	EZQ protein quantification kit	Thermo Fisher Scientific	Cat # R33200	For accurate protein quantification for proteomics

software, algorithm	MaxQuant	<a href="https://www.maxquant.org/">https://www.maxquant.org/</a>	RRID:SCR_014485	Version 1.6.3.3
software, algorithm	Limma	Ritchie et al., 2015	RRID:SCR_010943	Version 3.7
software, algorithm	Qvalue	Bioconductor	RRID:SCR_001073	Version 2.10
software, algorithm	FlowJo	Treestar		Version 10
software, algorithm	OMERO.figure	<a href="https://pypi.org/project/omero-figure/">https://pypi.org/project/omero-figure/</a>		Version 4.4.0
Other	RPMI 1640	Thermo Fisher Scientific/GIBCO	21875–034	Media to culture cells

424

## 425 **Mice**

426 All mice were bred and maintained with approval by the University of Dundee ethical review committee in  
427 compliance with U.K. Home Office Animals (Scientific Procedures) Act 1986 guidelines. C57BL/6J mice were  
428 purchased from Charles Rivers and acclimatised for a minimum of 10 days prior to use in experiments. Mice  
429 were maintained in a standard barrier facility on a 12hour light/dark cycle at 21°C, 45-65% relative humidity,  
430 in individually ventilated cages with corn cob and sizzler-nest material and fed an R&M3 diet (Special Diet  
431 Services, UK) and filtered water ad libitum. Cages were changed at least every two weeks. For all  
432 experiments mice were used between 8-12 weeks of age, and for proteomics, male mice aged 8-9 weeks  
433 were used.

434

## 435 **T-IEL and LN CD8 T cell isolation**

436 T-IEL were isolated for sorting from mice and as described in (James et al., 2020). Briefly, small intestines  
437 were extracted and flushed. Small intestines were longitudinally opened, then transversely cut into ~5 mm  
438 pieces and put into warm media containing 1mM DTT. Small intestine pieces were shaken for 40min,  
439 centrifuged, vortexed and passed through a 100µm sieve. The flow-through was centrifuged on a 36%/67%  
440 Percoll density gradient at 700g for 30 minutes. The T-IEL were isolated from the interface between 36% and  
441 67% Percoll. In some experiments, isolated T-IEL were further enriched using an EasySep™ Mouse CD8α  
442 positive selection kit (STEMCELL Technologies) as per the manufacturer's instructions. Isolation and sorting  
443 details for the LN and effector populations used for proteomics can be found at [www.lmmpres.co.uk](http://www.lmmpres.co.uk) under  
444 the 'Protocols & publications' tab.

445

## 446 **Proteomics sample preparation and peptide fractionation**

447 Sample preparation was done as in (Howden et al., 2019). Briefly, cell pellets were lysed, boiled and  
448 sonicated, and proteins purified using the SP3 method (Hughes et al., 2014). Proteins were digested with  
449 LysC and Trypsin and TMT labelling and peptide clean-up performed according to the SP3 protocol. The  
450 TMT labelling set up is available in Supplementary File 6. The TMT samples were fractionated using off-line  
451 high-pH reverse-phase chromatography: samples were loaded onto a 4.6 mm × 250 mm Xbridge BEH130  
452 C18 column with 3.5 µm particles (Waters). Using a Dionex BioRS system, the samples were separated  
453 using a 25-min multistep gradient of solvents A (10 mM formate at pH 9 in 2% acetonitrile) and B (10 mM  
454 ammonium formate at pH 9 in 80% acetonitrile), at a flow rate of 1 ml min<sup>-1</sup>. Peptides were separated into 48  
455 fractions, which were consolidated into 24 fractions. The fractions were subsequently dried, and the peptides  
456 were dissolved in 5% formic acid and analysed by liquid chromatography–mass spectrometry.

#### 457 458 **Liquid chromatography electrospray–tandem mass spectrometry analysis**

459 For each fraction, 1 µg was analysed using an Orbitrap Fusion Tribrid mass spectrometer (Thermo Fisher  
460 Scientific) equipped with a Dionex ultra-high-pressure liquid chromatography system (RSLCnano).  
461 Reversed-phase liquid chromatography was performed using a Dionex RSLCnano high-performance liquid  
462 chromatography system (Thermo Fisher Scientific). Peptides were injected onto a 75 µm × 2 cm PepMap-  
463 C18 pre-column and resolved on a 75 µm × 50 cm RP C18 EASY-Spray temperature-controlled integrated  
464 column-emitter (Thermo Fisher Scientific) using a 4-h multistep gradient from 5% B to 35% B with a constant  
465 flow of 200 nl min<sup>-1</sup>. The mobile phases were: 2% acetonitrile incorporating 0.1% formic acid (solvent A) and  
466 80% acetonitrile incorporating 0.1% formic acid (solvent B). The spray was initiated by applying 2.5 kV to the  
467 EASY-Spray emitter, and the data were acquired under the control of Xcalibur software in a data-dependent  
468 mode using the top speed and 4 s duration per cycle. The survey scan was acquired in the Orbitrap covering  
469 the *m/z* range from 400–1,400 Thomson units (Th), with a mass resolution of 120,000 and an automatic gain  
470 control (AGC) target of  $2.0 \times 10^5$  ions. The most intense ions were selected for fragmentation using collision-  
471 induced dissociation in the ion trap with 30% collision-induced dissociation energy and an isolation window  
472 of 1.6 Th. The AGC target was set to  $1.0 \times 10^4$ , with a maximum injection time of 70 ms and a dynamic  
473 exclusion of 80 s. During the MS3 analysis for more accurate TMT quantifications, ten fragment ions were  
474 co-isolated using synchronous precursor selection, a window of 2 Th and further fragmented using a higher-  
475 energy collisional dissociation energy of 55%. The fragments were then analysed in the Orbitrap with a  
476 resolution of 60,000. The AGC target was set to  $1.0 \times 10^5$  and the maximum injection time was set to 300 ms.

#### 477 478 **MaxQuant processing**

479 The raw proteomics data were analysed with MaxQuant (v. 1.6.3.3) (Cox and Mann, 2008; Tyanova et al.,  
480 2016) and searched against a hybrid database. The database contained all murine SwissProt entries, along  
481 with TrEMBL entries with a human paralog annotated within human SwissProt and with protein level  
482 evidence. The data was searched with the following modifications: carbamidomethylation of cysteine, as well  
483 as TMT modification on peptide amino termini and lysine side chains as fixed modifications; methionine  
484 oxidation and acetylation of amino termini of proteins were variable modifications. The false discovery rate  
485 was set to 1% at the protein and PSM level.

## 486 **Protein and BioReplicate filtering**

487 Proteins groups marked as 'Contaminants', 'Reverse' or 'Only identified by site' were filtered out.  
488 Additionally, proteins detected with less than 2 unique and razor peptides were also filtered out.  
489 Within both the TCR $\alpha\beta$  CD8 $\alpha\alpha$  and TCR $\alpha\beta$  CD8 $\alpha\beta$  T-IEL one replicate (replicate 4) was filtered out from the  
490 downstream analysis due to protein content discrepancies. This biorep displayed a 15% reduction in protein  
491 content compared to the other 3 replicates within the TCR $\gamma\delta$  CD8 $\alpha\alpha$  and an increase in protein content of  
492 32% when compared to the remaining 3 replicates within the TCR $\alpha\beta$  CD8 $\alpha\beta$ .

493

## 494 **Protein copy numbers and protein content**

495 Protein copy number were estimated from the MS data using the proteomic ruler (Wisniewski et al., 2014)  
496 after allocating the summed MS1 intensities to the different experimental conditions according to their  
497 fractional MS3 reporter intensities. The protein content was calculated based on copy numbers. The  
498 molecular weight (in Da) of each protein was multiplied by the number of copies for the corresponding  
499 protein and then divided by  $N_A$  (Avogadro's Constant) to yield the individual protein mass in  $\text{g cell}^{-1}$ . The  
500 individual masses were converted into picograms and then summed for all proteins to calculate the protein  
501 content.

502

## 503 **Differential expression and overrepresentation analyses**

504 All fold-changes and P-values for the individual proteins were calculated in R utilising the bioconductor  
505 package LIMMA version 3.7. The Q-values provided were generated in R using the "qvalue" package  
506 version 2.10.0. All other p-values were calculated using Welch's T-test. For all overrepresentation analyses  
507 (ORA) the background was set to the subset of proteins which were identified in either TCR $\alpha\beta$  CD8 $\alpha\beta$  T- IEL  
508 or in LN TCR $\alpha\beta$  CD8 $\alpha\beta$  T cells. The Gene Ontology ORAs were done using DAVID (Jiao et al., 2012) and  
509 PANTHER (Mi et al., 2019). Two distinct analyses were performed, one for proteins with a p-value <0.001  
510 and fold change greater than or equal to the median plus 1.5 standard deviations and a second one for  
511 proteins with a p-value <0.001 and fold change smaller than or equal to the median minus 1.5 standard  
512 deviations. The exhaustion ORA was done using WebGestalt (Wang et al., 2017) using the exhaustion  
513 markers provided reported within the literature (Khan et al., 2019) as a functional database for the analysis.

## 514 **Statistical significance thresholds**

515 For the bar and box plots, symbols on bars represent independent biological replicates. For the mass  
516 spectrometry derived bar plots and heatmaps ; \*\* = p-value < 0.001 and fold change greater than or equal to  
517 the median plus 1 standard deviation, \*\*\* = p-value < 0.0001 and fold change greater than or equal to the  
518 median +/- 1.5 standard deviations, based on the differential expression analyses described above. For all  
519 plots with non-MS based data, statistical analyses were carried out using R and GraphPad Prism v.8. The  
520 exact tests used are described in the figure legends, and p-values < 0.05 were considered significant.

## 521 **Flow cytometry**

522 Cells were stained with titrated concentrations of the following murine monoclonal antibodies: TCR $\beta$  [clone  
523 H57-597 (BioLegend)], TCR $\gamma\delta$  [clone GL3 (BioLegend or eBioscience)], CD4 [clone RM4-5 (BioLegend)],  
524 CD8 $\alpha$  [clone 53-6.7 (BioLegend)], CD8 $\beta$  [clone H35-17.2 (eBioscience)], CD103 [clone 2E7 (BioLegend)],  
525 CD39 [clone Duha59 (BioLegend)], CD73 [clone Ty/11.8 (BioLegend)], CD38 [clone 90 (BioLegend)], P2X7R

526 [clone 1F11 (BioLegend)], CD244 [clone eBio244F4 (eBioscience)], LAG-3 [(clone eBioC9B7W)], CD160  
 527 [clone 7H1 (BioLegend)], CD96 [clone 3.3 (BioLegend)], EpCAM [clone G8.8 (eBioscience)], E-Cadherin  
 528 [clone DECMA-1 (eBioscience)], TOX [clone TXRX10 (eBioscience)]. All data was acquired on a LSR  
 529 Fortessa flow cytometer with DIVA software (BD Biosciences). Data were analysed using FlowJo software  
 530 v10 (TreeStar).

531 For TCR stimulation, T-IEL and LN T cells were isolated and enriched for CD8+ as described above. T-IEL  
 532 were stained with Live/Dead fixable Near-IR (ThermoFisher) (1:250) for 10 min prior to stimulation then  
 533 combined with LN T cells at a 1:1 ratio and resuspended at a concentration of  $10^6$  cells/ml in RPMI  
 534 containing 1% FBS, L-Glutamine and Penicillin/Streptomycin. Cells were warmed at 37°C before being  
 535 stimulated with 30µg/ml of anti-CD3 antibody [clone 145-2C11 (BioLegend)] and 5µg/ml of polyclonal anti-  
 536 hamster crosslinking antibody (Jackson ImmunoResearch) for 5 min at 37°C. For some samples as  
 537 indicated, PP2 was added at a concentration of 20µM for 1 hour prior to stimulation. After stimulation cells  
 538 were directly fixed in 2% PFA 10 min at 37°C before permeabilization with 90% ice cold methanol. Samples  
 539 were then fluorescently barcoded with different concentration (0, 11.1, 33.3 or 100µg/ml) of the Pacific Blue  
 540 Dye (ThermoFisher) for 40 min, on ice before quenching with PBS+ 0.5% BSA (v:v). Barcoded samples were  
 541 then pooled and stained for intracellular phospho-proteins, phospho-p44/42 MAPK (Erk1/2) (Thr202/Tyr204)  
 542 [Clone 197G2 (Cell Signalling Technologies)] and phospho-S6 ribosomal protein (Ser235/236) [Clone  
 543 D57.2.2E (Cell Signalling Technologies)] for 30 min at RT, protected from light, followed by secondary  
 544 DyLight649 antibody (BioLegend). Cells were then stained for surface markers. Data were acquired using  
 545 CytoFlex flow cytometer and analysed using FlowJo software (v10). Data were analysed using the "Forward  
 546 deconvolution method" described in [\(Krutzik and Nolan, 2006\)](#). Briefly, samples were differentiated based in  
 547 the fluorescence intensities of each dye and then individual samples were analysed for their respective  
 548 phospho-protein expression.

549

#### 550 **Protein synthesis measurements**

551 For comparing rates of protein synthesis, T-IEL and LN single cell suspensions were cultured with 20µM O-  
 552 propargyl-puromycin (OPP) (JenaBioscience) for 15 minutes. As a negative control, cells were pre-treated  
 553 with 0.1mg/mL cycloheximide (CHX) for 15 minutes before adding the OPP for 15 minutes (30m total CHX  
 554 exposure). Cells were then harvested, fixed with 4% paraformaldehyde (PFA) and permeabilised with 0.5 %  
 555 triton X-100 before undergoing a copper catalysed click chemistry reaction with Alexa 647-azide (Sigma).  
 556 Following surface marker staining, cells were resuspended in PBS + 1% BSA and analysed by flow  
 557 cytometry to determine the degree of incorporation of OPP. All samples were acquired on a LSR Fortessa  
 558 flow cytometer with DIVA software (BD Biosciences). Data were analysed using FlowJo software.

#### 559 **Cellular cholesterol measurements**

560 Cholesterol content was measured using the Amplex Red cholesterol Assay Kit (Invitrogen). T-IEL were  
 561 sorted into TCRβ+CD8αα+, TCRβ+CD8αβ+ and TCRγδ+CD8αα+ populations and LN cells were sorted for  
 562 TCRβ+CD8αβ CD44-lo CD62L-hi cells using the BD Influx Cell Sorter (BD Biosciences). Each population  
 563 was lysed at a concentration of  $10 \times 10^6$  cells/ml in 1X Amplex Red reaction buffer (Invitrogen) for 10 minutes  
 564 at 4°C then spun at 13,200 rpm for 12 minutes. Lysate was removed and diluted in 1X Amplex Red reaction  
 565 buffer. 50 µl of 300 µM Amplex Red reagent (containing 2 U/ml horseradish peroxidase, 2 U/ml cholesterol



oxidase and 0.2 U/ml cholesterol esterase) was added to 50 µl of diluted lysate. The reaction was incubated for 30 minutes at 37°C in the dark before reading on the Clariostar microplate reader (BMG Labtech) at excitation wavelength of 530 nm and emission wavelength of 590nm. Cholesterol content in the lysates was calculated with reference to cholesterol standards.

## Immunofluorescence and imaging

T-IEL and LN T cells were isolated and enriched for CD8+ as described above. T-IEL were then washed twice in RPMI/10%FBS-containing media and further depleted of contaminating dead cells using EasySep™ Dead Cell Removal (Annexin V) Kit (STEMCELL Technologies) as per manufacturer instructions, for negative enrichment of T-IEL. The purity and viability were checked by flow cytometry with CD8α-APC antibody and DAPI. LN CD8 T cells were at >98% purity, and the IEL were enriched to 60% purity.

1x10<sup>6</sup> lymphocytes in PBS were gravity-sedimented onto each 18 mm round coverslip (N1.5) as described (Tsang et al., 2017). Cells were fixed in 3.7% PFA in PBS, pH=7.4, for 10 min at room temperature, washed with PBS, permeabilised with 0.5% Triton X-100 in PBS for 15 min, washed with PBS and blocked with 2% bovine serum albumin and 0.1% Triton X-100 in PBS for 45 min prior to staining with primary antibodies diluted as indicated below in blocking solution, or blocking solution alone, for 1h 45 min at room temperature. Antibodies used were polyclonal rabbit anti-ZO-2 (Cell Signalling Technologies) used at 1:50 dilution, mouse monoclonal anti-E-cadherin (BD Biosciences), used at 1:100 dilution, rat monoclonal anti-CD8α-FITC [clone 53-6.7, (Biolegend), used at 1:100]. After three washes with PBS cells were further incubated with appropriate secondary antibodies diluted 1:500 in blocking solution for 1 h. Secondary antibodies used were goat anti-rat-AlexaFluor488 (Invitrogen); goat anti-mouse-AlexaFluor568 (Invitrogen); donkey anti-rabbit-AlexaFluor647 (Jackson ImmunoResearch). After additional 3 washes with PBS cells were stained with 1 µg/ml DAPI in PBS for 10-15 min, washed with PBS and mounted onto glass slides using ProLong gold antifade reagent (Thermo Fisher Scientific) as a mounting media. Stained cells were imaged using LSM 710 confocal microscope operated by Zen software (Zeiss) with a 63x/1.4NA oil immersion objective. For each image, 7-12 optical sections spanning the entire thickness of the cells were collected. The maximal intensity projections were generated and intensities adjusted in identical manner for all images in OMERO using the OMERO.figure app (Allan et al., 2012).

## Data availability

The raw and processed mass spectrometry proteomics data have been deposited to the ProteomeXchange Consortium via the PRIDE partner repository (Perez-Riverol et al., 2019) with the dataset identifier PXD023140 (<https://www.ebi.ac.uk/pride/archive/projects/PXD023140/>). All other data generated in this study are included within the manuscript and supporting files.

## References

- Alfei F, Kanev K, Hofmann M, Wu M, Ghoneim HE, Roelli P, Utzschneider DT, von Hoesslin M, Cullen JG, Fan Y, Eisenberg V, Wohlleber D, Steiger K, Merkler D, Delorenzi M, Knolle PA, Cohen CJ, Thimme R, Youngblood B, Zehn D. 2019. TOX reinforces the phenotype and longevity of exhausted T cells in chronic viral infection. *Nature* **571**:265–269. doi:10.1038/s41586-019-1326-9
- Allan C, Burel J-M, Moore J, Blackburn C, Linkert M, Loynton S, MacDonald D, Moore WJ, Neves C, Patterson A, Porter M, Tarkowska A, Loranger B, Avondo J, Lagerstedt I, Lianas L, Leo S, Hands K,

Hay RT, Patwardhan A, Best C, Kleywegt GJ, Zanetti G, Swedlow JR. 2012. OMERO: flexible, model-driven data management for experimental biology. *Nat Methods* **9**:245–253. doi:10.1038/nmeth.1896

Argüello RJ, Combes AJ, Char R, Gigan J-P, Baaziz AI, Bousiquot E, Camosseto V, Samad B, Tsui J, Yan P, Boissonneau S, Figarella-Branger D, Gatti E, Tabouret E, Krummel MF, Pierre P. 2020. SCENITH: A Flow Cytometry-Based Method to Functionally Profile Energy Metabolism with Single-Cell Resolution. *Cell Metabolism* **32**:1063-1075.e7. doi:10.1016/j.cmet.2020.11.007

Borges da Silva H, Beura LK, Wang H, Hanse EA, Gore R, Scott MC, Walsh DA, Block KE, Fonseca R, Yan Y, Hippen KL, Blazar BR, Masopust D, Kelekar A, Vulchanova L, Hogquist KA, Jameson SC. 2018. The purinergic receptor P2RX7 directs metabolic fitness of long-lived memory CD8+ T cells. *Nature* **559**:264–268. doi:10.1038/s41586-018-0282-0

Cheng H-Y, Wu R, Gebre AK, Hanna RN, Smith DJ, Parks JS, Ley K, Hedrick CC. 2013. Increased Cholesterol Content in Gammadelta ( $\gamma\delta$ ) T Lymphocytes Differentially Regulates Their Activation. *PLOS ONE* **8**:e63746. doi:10.1371/journal.pone.0063746

Cox J, Mann M. 2008. MaxQuant enables high peptide identification rates, individualized p.p.b.-range mass accuracies and proteome-wide protein quantification. *Nat Biotechnol* **26**:1367–72. doi:10.1038/nbt.1511

Delgado M, Pozo D, Ganea D. 2004. The Significance of Vasoactive Intestinal Peptide in Immunomodulation. *Pharmacol Rev* **56**:249–290.

Denning TL, Granger SW, Granger S, Mucida D, Graddy R, Leclercq G, Zhang W, Honey K, Rasmussen JP, Cheroutre H, Rudensky AY, Kronenberg M. 2007. Mouse TCR $\alpha\beta$ +CD8 $\alpha\alpha$  intraepithelial lymphocytes express genes that down-regulate their antigen reactivity and suppress immune responses. *Journal of immunology (Baltimore, Md : 1950)* **178**:4230–4239. doi:10.4049/jimmunol.178.7.4230

Di Marco Barros R, Roberts NA, Dart RJ, Vantourout P, Jandke A, Nussbaumer O, Deban L, Cipolat S, Hart R, Iannitto ML, Laing A, Spencer-Dene B, East P, Gibbons D, Irving PM, Pereira P, Steinhoff U, Hayday A. 2016. Epithelia Use Butyrophilin-like Molecules to Shape Organ-Specific  $\gamma\delta$  T Cell Compartments. *Cell* **167**:203-218.e17. doi:10.1016/j.cell.2016.08.030

Fahrer AM, Konigshofer Y, Kerr EM, Ghandour G, Mack DH, Davis MM, Chien Y. 2001. Attributes of  $\gamma\delta$  intraepithelial lymphocytes as suggested by their transcriptional profile. *Proceedings of the National Academy of Sciences of the United States of America* **98**:10261–10266. doi:10.1073/pnas.171320798

Frizzell H, Fonseca R, Christo SN, Evrard M, Cruz-Gomez S, Zanluqui NG, von Scheidt B, Freestone D, Park SL, McWilliam HEG, Villadangos JA, Carbone FR, Mackay LK. 2020. Organ-specific isoform selection of fatty acid-binding proteins in tissue-resident lymphocytes. *Sci Immunol* **5**:eaay9283. doi:10.1126/sciimmunol.aay9283

Fuller DM, Zhu M, Ou-Yang C-W, Sullivan SA, Zhang W. 2011. A tale of two TRAPs: LAT and LAB in the regulation of lymphocyte development, activation, and autoimmunity. *Immunol Res* **49**:97–108. doi:10.1007/s12026-010-8197-3

Gaud G, Lesourne R, Love PE. 2018. Regulatory mechanisms in T cell receptor signalling. *Nat Rev Immunol* **18**:485–497. doi:10.1038/s41577-018-0020-8

Geiger R, Rieckmann JC, Wolf T, Basso C, Feng Y, Fuhrer T, Kogadeeva M, Picotti P, Meissner F, Mann M, Zamboni N, Sallusto F, Lanzavecchia A. 2016. L-Arginine Modulates T Cell Metabolism and Enhances Survival and Anti-tumor Activity. *Cell* **167**:829-842.e13. doi:10.1016/j.cell.2016.09.031

Geltink RIK, Kyle RL, Pearce EL. 2018. Unraveling the Complex Interplay Between T Cell Metabolism and Function. *Annu Rev Immunol* **36**:461–488. doi:10.1146/annurev-immunol-042617-053019

Gomes I, Aryal DK, Wardman JH, Gupta A, Gagnidze K, Rodriguiz RM, Kumar S, Wetsel WC, Pintar JE, Fricker LD, Devi LA. 2013. GPR171 is a hypothalamic G protein-coupled receptor for BigLEN, a neuropeptide involved in feeding. *Proc Natl Acad Sci U S A* **110**:16211–16216. doi:10.1073/pnas.1312938110

He S, Kahles F, Rattik S, Nairz M, McAlpine CS, Anzai A, Selgrade D, Fenn AM, Chan CT, Mindur JE, Valet C, Poller WC, Halle L, Rotllan N, Iwamoto Y, Wojtkiewicz GR, Weissleder R, Libby P, Fernández-Hernando C, Drucker DJ, Nahrendorf M, Swirski FK. 2019. Gut intraepithelial T cells calibrate metabolism and accelerate cardiovascular disease. *Nature* **566**:115–119. doi:10.1038/s41586-018-0849-9

Howden AJM, Hukelmann JL, Brenes A, Spinelli L, Sinclair LV, Lamond AI, Cantrell DA. 2019. Quantitative analysis of T cell proteomes and environmental sensors during T cell differentiation. *Nat Immunol* **20**:1542–1554. doi:10.1038/s41590-019-0495-x

Hughes CS, Foehr S, Garfield DA, Furlong EE, Steinmetz LM, Krijgsveld J. 2014. Ultrasensitive proteome analysis using paramagnetic bead technology. *Mol Syst Biol* **10**:757. doi:10.15252/msb.20145625

Hussain MM, Rava P, Walsh M, Rana M, Iqbal J. 2012. Multiple functions of microsomal triglyceride transfer protein. *Nutr Metab (Lond)* **9**:14. doi:10.1186/1743-7075-9-14

- 667 Inagaki-Ohara K, Sawaguchi A, Suganuma T, Matsuzaki G, Nawa Y. 2005. Intraepithelial lymphocytes  
668 express junctional molecules in murine small intestine. *Biochemical and biophysical research*  
669 *communications* **331**:977–983. doi:10.1016/j.bbrc.2005.04.025
- 670 James OJ, Vandereyken M, Swamy M. 2020. Isolation, Characterization, and Culture of Intestinal  
671 Intraepithelial Lymphocytes. *Methods in molecular biology (Clifton, NJ)* **2121**:141–152.  
672 doi:10.1007/978-1-0716-0338-3\_13
- 673 James OJ, Vandereyken M, Marchingo JM, Singh F, Bray SE, Wilson J, Love AG, Swamy M. 2021. IL-15  
674 and PIM kinases direct the metabolic programming of intestinal intraepithelial lymphocytes. *Nat*  
675 *Commun* **12**:4290. doi:10.1038/s41467-021-24473-2
- 676 Jiao X, Sherman BT, Huang DW, Stephens R, Baseler MW, Lane HC, Lempicki RA. 2012. DAVID-WS: a  
677 stateful web service to facilitate gene/protein list analysis. *Bioinformatics* **28**:1805–1806.  
678 doi:10.1093/bioinformatics/bts251
- 679 Khan O, Giles JR, McDonald S, Manne S, Ngiow SF, Patel KP, Werner MT, Huang AC, Alexander KA, Wu  
680 JE, Attanasio J, Yan P, George SM, Bengsch B, Staupe RP, Donahue G, Xu W, Amaravadi RK, Xu  
681 X, Karakousis GC, Mitchell TC, Schuchter LM, Kaye J, Berger SL, Wherry EJ. 2019. TOX  
682 transcriptionally and epigenetically programs CD8<sup>+</sup> T cell exhaustion. *Nature* **571**:211–218.  
683 doi:10.1038/s41586-019-1325-x
- 684 Konjar Š, Frising UC, Ferreira C, Hinterleitner R, Mayassi T, Zhang Q, Blankenhaus B, Haberman N, Loo Y,  
685 Guedes J, Baptista M, Innocentin S, Stange J, Strathdee D, Jabri B, Veldhoen M. 2018.  
686 Mitochondria maintain controlled activation state of epithelial-resident T lymphocytes. *Science*  
687 *Immunology* **3**:aan2543. doi:10.1126/sciimmunol.aan2543
- 688 Li Y, Innocentin S, Withers DR, Roberts NA, Gallagher AR, Grigorieva EF, Wilhelm C, Veldhoen M. 2011.  
689 Exogenous stimuli maintain intraepithelial lymphocytes via aryl hydrocarbon receptor activation. *Cell*  
690 **147**:629–640. doi:10.1016/j.cell.2011.09.025
- 691 Ma EH, Verway MJ, Johnson RM, Roy DG, Steadman M, Hayes S, Williams KS, Sheldon RD, Samborska B,  
692 Kosinski PA, Kim H, Griss T, Faubert B, Condotta SA, Krawczyk CM, DeBerardinis RJ, Stewart KM,  
693 Richer MJ, Chubukov V, Roddy TP, Jones RG. 2019. Metabolic Profiling Using Stable Isotope  
694 Tracing Reveals Distinct Patterns of Glucose Utilization by Physiologically Activated CD8<sup>+</sup> T Cells.  
695 *Immunity* **51**:856-870.e5. doi:10.1016/j.immuni.2019.09.003
- 696 Madison BB. 2016. Srebp2: A master regulator of sterol and fatty acid synthesis. *Journal of Lipid Research*  
697 **57**:333–335. doi:10.1194/jlr.C066712
- 698 Malinarich FH, Grabski E, Worbs T, Chennupati V, Haas JD, Schmitz S, Candia E, Quera R, Malissen B,  
699 Förster R, Hermoso M, Prinz I. 2010. Constant TCR triggering suggests that the TCR expressed on  
700 intestinal intraepithelial  $\gamma\delta$  T cells is functional in vivo. *European Journal of Immunology* **40**:3378–  
701 3388. doi:10.1002/eji.201040727
- 702 Marchingo JM, Sinclair LV, Howden AJ, Cantrell DA. 2020. Quantitative analysis of how Myc controls T cell  
703 proteomes and metabolic pathways during T cell activation. *eLife* **9**:e53725. doi:10.7554/eLife.53725
- 704 Martí i Líndez A-A, Dunand-Sauthier I, Conti M, Gobet F, Núñez N, Hannich JT, Riezman H, Geiger R,  
705 Piersigilli A, Hahn K, Lemeille S, Becher B, De Smedt T, Hugues S, Reith W. 2019. Mitochondrial  
706 arginase-2 is a cell-autonomous regulator of CD8<sup>+</sup> T cell function and antitumor efficacy. *JCI Insight*  
707 **4**:132975. doi:10.1172/jci.insight.132975
- 708 Mi H, Muruganujan A, Huang X, Ebert D, Mills C, Guo X, Thomas PD. 2019. Protocol Update for large-scale  
709 genome and gene function analysis with the PANTHER classification system (v.14.0). *Nat Protoc*  
710 **14**:703–721. doi:10.1038/s41596-019-0128-8
- 711 Molnár E, Swamy M, Holzer M, Beck-García K, Worch R, Thiele C, Guigas G, Boye K, Luescher IF, Schwiller  
712 P, Schubert R, Schamel WWA. 2012. Cholesterol and Sphingomyelin Drive Ligand-independent T-  
713 cell Antigen Receptor Nanoclustering. *Journal of Biological Chemistry* **287**:42664–42674.  
714 doi:10.1074/jbc.M112.386045
- 715 Mráček T, Drahota Z, Houštěk J. 2013. The function and the role of the mitochondrial glycerol-3-phosphate  
716 dehydrogenase in mammalian tissues. *Biochimica et Biophysica Acta (BBA) - Bioenergetics*  
717 **1827**:401–410. doi:10.1016/j.bbabo.2012.11.014
- 718 Nochi T, Yuki Y, Terahara K, Hino A, Kunisawa J, Kweon M-N, Yamaguchi T, Kiyono H. 2004. Biological role  
719 of Ep-CAM in the physical interaction between epithelial cells and lymphocytes in intestinal  
720 epithelium. *Clinical immunology (Orlando, Fla)* **113**:326–339. doi:10.1016/j.clim.2004.08.013
- 721 Olivares-Villagómez D, Van Kaer L. 2018. Intestinal Intraepithelial Lymphocytes: Sentinels of the Mucosal  
722 Barrier. *Trends in immunology* **39**:264–275. doi:10.1016/j.it.2017.11.003
- 723 Pan X, Hussain MM. 2012. Gut triglyceride production. *Biochimica et Biophysica Acta (BBA) - Molecular and*  
724 *Cell Biology of Lipids* **1821**:727–735. doi:10.1016/j.bbalip.2011.09.013
- 725 Pan Y, Tian T, Park CO, Lofftus SY, Mei S, Liu X, Luo C, O'Malley JT, Gehad A, Teague JE, Divito SJ,  
726 Fuhlbrigge R, Puigserver P, Krueger JG, Hotamisligil GS, Clark RA, Kupper TS. 2017. Survival of

tissue-resident memory T cells requires exogenous lipid uptake and metabolism. *Nature* **543**:252–256. doi:10.1038/nature21379

Perez-Riverol Y, Csordas A, Bai J, Bernal-Llinares M, Hewapathirana S, Kundu DJ, Inuganti A, Griss J, Mayer G, Eisenacher M, Pérez E, Uszkoreit J, Pfeuffer J, Sachsenberg T, Yilmaz S, Tiwary S, Cox J, Audain E, Walzer M, Jarnuczak AF, Ternent T, Brazma A, Vizcaino JA. 2019. The PRIDE database and related tools and resources in 2019: improving support for quantification data. *Nucleic Acids Res* **47**:D442–D450. doi:10.1093/nar/gky1106

Romero-Gomez M, Jover M, Galan JJ, Ruiz A. 2009. Gut ammonia production and its modulation. *Metab Brain Dis* **24**:147–57. doi:10.1007/s11011-008-9124-3

Ron-Harel N, Ghergurovich JM, Notarangelo G, LaFleur MW, Tsubosaka Y, Sharpe AH, Rabinowitz JD, Haigis MC. 2019. T Cell Activation Depends on Extracellular Alanine. *Cell Reports* **28**:3011–3021.e4. doi:10.1016/j.celrep.2019.08.034

Sasson SC, Gordon CL, Christo SN, Klenerman P, Mackay LK. 2020. Local heroes or villains: tissue-resident memory T cells in human health and disease. *Cell Mol Immunol* **17**:113–122. doi:10.1038/s41423-019-0359-1

Schietinger A, Philip M, Krisnawan VE, Chiu EY, Delrow JJ, Basom RS, Lauer P, Brockstedt DG, Knoblaugh SE, Hämmerling GJ, Schell TD, Garbi N, Greenberg PD. 2016. Tumor-Specific T Cell Dysfunction Is a Dynamic Antigen-Driven Differentiation Program Initiated Early during Tumorigenesis. *Immunity* **45**:389–401. doi:10.1016/j.immuni.2016.07.011

Scott AC, Dündar F, Zumbo P, Chandran SS, Klebanoff CA, Shakiba M, Trivedi P, Menocal L, Appleby H, Camara S, Zamarin D, Walther T, Snyder A, Femia MR, Comen EA, Wen HY, Hellmann MD, Anandasabapathy N, Liu Y, Altorki NK, Lauer P, Levy O, Glickman MS, Kaye J, Betel D, Philip M, Schietinger A. 2019. TOX is a critical regulator of tumour-specific T cell differentiation. *Nature* **571**:270–274. doi:10.1038/s41586-019-1324-y

Seillet C, Luong K, Tellier J, Jacquilot N, Shen RD, Hickey P, Wimmer VC, Whitehead L, Rogers K, Smyth GK, Garnham AL, Ritchie ME, Belz GT. 2020. The neuropeptide VIP confers anticipatory mucosal immunity by regulating ILC3 activity. *Nat Immunol* **21**:168–177. doi:10.1038/s41590-019-0567-y

Shires J, Theodoridis E, Hayday AC. 2001. Biological insights into TCRgammadelta+ and TCRalphabeta+ intraepithelial lymphocytes provided by serial analysis of gene expression (SAGE). *Immunity* **15**:419–434.

Sinclair LV, Howden AJ, Brenes A, Spinelli L, Hukelmann JL, Macintyre AN, Liu X, Thomson S, Taylor PM, Rathmell JC, Locasale JW, Lamond AI, Cantrell DA. 2019. Antigen receptor control of methionine metabolism in T cells. *eLife* **8**:e44210. doi:10.7554/eLife.44210

Spinelli JB, Haigis MC. 2018. The multifaceted contributions of mitochondria to cellular metabolism. *Nat Cell Biol* **20**:745–754. doi:10.1038/s41556-018-0124-1

Stark R, Wesselink TH, Behr FM, Kragten NAM, Arens R, Koch-Nolte F, van Gisbergen KPJM, van Lier RAW. 2018. **T<sub>RM</sub> maintenance is regulated by tissue damage via P2RX7**. *Sci Immunol* **3**:eaau1022. doi:10.1126/sciimmunol.aau1022

Stockinger B, Meglio PD, Gialitakis M, Duarte JH. 2014. The Aryl Hydrocarbon Receptor: Multitasking in the Immune System. *Annu Rev Immunol* **32**:403–432. doi:10.1146/annurev-immunol-032713-120245

Talbot J, Hahn P, Kroehling L, Nguyen H, Li D, Littman DR. 2020. Feeding-dependent VIP neuron–ILC3 circuit regulates the intestinal barrier. *Nature* **579**:575–580. doi:10.1038/s41586-020-2039-9

Tanos R, Patel RD, Murray IA, Smith PB, Patterson AD, Perdew GH. 2012. Aryl hydrocarbon receptor regulates the cholesterol biosynthetic pathway in a dioxin response element-independent manner. *Hepatology* **55**:1994–2004. doi:10.1002/hep.25571

Tsang M, Gantchev J, Ghazawi FM, Litvinov IV. 2017. Protocol for adhesion and immunostaining of lymphocytes and other non-adherent cells in culture. *BioTechniques* **63**. doi:10.2144/000114610

Tyanova S, Temu T, Cox J. 2016. The MaxQuant computational platform for mass spectrometry-based shotgun proteomics. *Nat Protoc* **11**:2301–2319. doi:10.1038/nprot.2016.136

Vandereyken M, James OJ, Swamy M. 2020. Mechanisms of activation of innate-like intraepithelial T lymphocytes. *Mucosal Immunology* **13**:721–731. doi:10.1038/s41385-020-0294-6

Wang J, Vasaiikar S, Shi Z, Greer M, Zhang B. 2017. WebGestalt 2017: a more comprehensive, powerful, flexible and interactive gene set enrichment analysis toolkit. *Nucleic Acids Research* **45**:W130–W137. doi:10.1093/nar/gkx356

Wencker M, Turchinovich G, Di Marco Barros R, Deban L, Jandke A, Cope A, Hayday AC. 2014. Innate-like T cells straddle innate and adaptive immunity by altering antigen-receptor responsiveness. *Nat Immunol* **15**:80–87. doi:10.1038/ni.2773

Wisniewski JR, Hein MY, Cox J, Mann M. 2014. A “proteomic ruler” for protein copy number and concentration estimation without spike-in standards. *Mol Cell Proteomics* **13**:3497–506. doi:10.1074/mcp.M113.037309

787 Wolf T, Jin W, Zoppi G, Vogel IA, Akhmedov M, Bleck CKE, Beltraminelli T, Rieckmann JC, Ramirez NJ,  
 788 Benevento M, Notarbartolo S, Bumann D, Meissner F, Grimbacher B, Mann M, Lanzavecchia A,  
 789 Sallusto F, Kwee I, Geiger R. 2020. Dynamics in protein translation sustaining T cell preparedness.  
 790 *Nat Immunol* **21**:927–937. doi:10.1038/s41590-020-0714-5  
 791 Yang W, Bai Y, Xiong Y, Zhang J, Chen S, Zheng X, Meng X, Li L, Wang J, Xu Chenguang, Yan C, Wang L,  
 792 Chang CCY, Chang T-Y, Zhang T, Zhou P, Song B-L, Liu W, Sun S, Liu X, Li B, Xu Chenqi. 2016.  
 793 Potentiating the antitumour response of CD8+ T cells by modulating cholesterol metabolism. *Nature*  
 794 **531**:651–655. doi:10.1038/nature17412  
 795 Yen C-LE, Nelson DW, Yen M-I. 2015. Intestinal triacylglycerol synthesis in fat absorption and systemic  
 796 energy metabolism. *Journal of Lipid Research* **56**:489–501. doi:10.1194/jlr.R052902  
 797 Yoo BB, Mazmanian SK. 2017. The Enteric Network: Interactions between the Immune and Nervous  
 798 Systems of the Gut. *Immunity* **46**:910–926. doi:10.1016/j.immuni.2017.05.011  
 799 Yusta B, Baggio LL, Koehler J, Holland D, Cao X, Pinnell LJ, Johnson-Henry KC, Yeung W, Surette MG,  
 800 Bang KA, Sherman PM, Drucker DJ. 2015. GLP-1 receptor (GLP-1R) agonists modulate enteric  
 801 immune responses through the intestinal intraepithelial lymphocyte (IEL) GLP-1R. *Diabetes*  
 802 **64**:db141577-2549. doi:10.2337/db14-1577  
 803

804

805 **Figure 1: Quantitative proteomic analyses of induced and natural T-IEL subsets**

806 **(a)** Schematic of the MS based proteomics workflow. The data were acquired at the MS3 level with  
807 synchronous precursor selection (see methods). **(b)** Principal component analysis comparing the TMT based  
808 estimated protein copy numbers of conventional naïve and effector T cells with T-IEL. CTL, Cytotoxic T  
809 lymphocytes. **(c)** Bar plot showing the number of proteins identified across all replicates in the 5 populations  
810 used for this study. **(d)** Box plot showing the MS based protein content estimation for all replicates used  
811 across the 5 populations. **(e)** Principal component analysis comparing the estimated protein copy numbers  
812 across conventional naïve LN T cells and T-IEL subsets. **(f-i)** Scatter plot comparing the estimated copy  
813 numbers for **(f)** TCRαβ<sup>+</sup> CD8αβ<sup>+</sup> T-IEL and WT LN TCRαβ CD8αβ T cells, **(g)** TCRαβ<sup>+</sup> CD8αβ<sup>+</sup> T-IEL and  
814 TCRαβ<sup>+</sup> CD8αα<sup>+</sup> T-IEL, **(h)** TCRαβ<sup>+</sup> CD8αβ<sup>+</sup> T-IEL and TCRγδ<sup>+</sup> CD8αα<sup>+</sup> T-IEL, **(i)** WT LN TCRαβ CD8αβ T  
815 cells and p14 LN TCRαβ CD8αβ T cells. Pearson correlation coefficient are included within all the scatter  
816 plots. The proteomics data displayed on the plots include CTL (n=3 biological replicates), conventional naïve  
817 LN T cells (both WT and p14 n=6 biological replicates), TCRαβ<sup>+</sup> CD8αβ<sup>+</sup> T-IEL and TCRαβ<sup>+</sup> CD8αα<sup>+</sup> T-IEL  
818 (n=3 biological replicates) and TCRγδ<sup>+</sup> CD8αα<sup>+</sup> T-IEL (n= 4 biological replicates). For boxplots, the bottom  
819 and top hinges represent the 1<sup>st</sup> and 3<sup>rd</sup> quartiles. The top whisker extends from the hinge to the largest  
820 value no further than 1.5 × IQR from the hinge; the bottom whisker extends from the hinge to the smallest  
821 value at most 1.5 × IQR of the hinge. The bar plots show the mean. Total number of proteins identified and  
822 total protein content across all populations are available in Figure 1-source data 1.

823 **Figure 1- source data 1: Total protein identifications and total protein content across all populations**

824 **Figure 1- figure supplement 1. Gating strategy used to identify and isolate T-IEL subsets using**  
825 **fluorescence activated cell sorting (FACS).** Lymphocytes were gated by size using forward scatter (FCS)  
826 and side scatter (SSC) and T-IEL subsets were separated based on the cell surface marker expression of T  
827 cell-associated receptors: TCRβ, TCRγδ, CD8α, CD8β and CD4. The populations sorted were as followed:  
828 cells positive for TCRγδ and CD8αα (TCRγδ CD8αα T-IEL), and those that were both TCRβ<sup>+</sup> and CD4<sup>-</sup> and  
829 either CD8αα (TCRβ CD8αα T-IEL) or CD8β (TCRβ CD8αβ T-IEL).

830 **Figure 2: Gene ontology analyses of the induced T-IEL proteome**

831 **(a)** Treemap showing the abundance of proteins classified into histones, ribosomal proteins, cytoskeletal  
832 proteins, glycolytic enzymes, chaperones and granzymes across WT LN TCRαβ CD8αβ T cells and TCRαβ<sup>+</sup>  
833 CD8αβ<sup>+</sup> T-IEL. Rectangle size is proportional to the median estimated copy numbers. Median copy numbers  
834 across all categories are available in Figure 2-source data 1. **(b)** Bar plots showing the estimated copy  
835 numbers for all granzymes across WT LN TCRαβ CD8αβ T cells (n=6) and all T-IEL (n=3 or 4). Symbols on  
836 the bars represent the biological replicates. The bars show the mean and SEM. p-values have been  
837 calculated on R with LIMMA where \*\*= p <0.001 and fold change greater than or equal to the median plus 1  
838 standard deviation, \*\*\*= p <0.0001 and fold change greater than or equal to the median +/- 1.5 standard  
839 deviations. **(c)** Bar plot showing the results of the DAVID functional annotation clustering (FDR<0.05; see  
840 methods for details) enrichment analysis for all proteins exclusive to or significantly increased in expression  
841 within TCRαβ<sup>+</sup> CD8αβ<sup>+</sup> T-IEL. **(d)** Bar plot showing the results of the PANTHER GO Biological process  
842 (FDR<0.05; see methods for details) enrichment analysis for all proteins exclusive to or significantly  
843 increased in expression within TCRαβ<sup>+</sup> CD8αβ<sup>+</sup> T-IEL (blue) or within WT TCRαβ CD8αβ T cells (red).

844 **Figure 2-source data 1: Median copy numbers for the global analysis**

845 **Figure 3: Downregulation of protein synthesis in T-IEL**

846 **(a)** Box plots showing the estimated total cytoplasmic (left) and mitochondrial (right) ribosomal protein copies  
847 for LN TCR $\beta$  CD8 $\alpha\beta$  T cells and all T-IEL subsets. The sums of all copy numbers are available in Figure 3-  
848 source data 1. **(b)** Box plots showing the estimated summed total protein copies for the protein subunits that  
849 are exclusive to RNA Polymerases I, II and III, respectively for LN TCR $\beta$  CD8 $\alpha\beta$  T cells and all T-IEL  
850 subsets. The sum of all copy numbers are available in Figure 3-source data 1. **(c)** Bar plots showing the  
851 estimated protein copy numbers of the amino acid transporters, SLC7A5 and SLC38A2, for WT LN TCR $\beta$   
852 CD8 $\alpha\beta$  and all 3 subsets of T-IEL. **(d)** Bar plots showing the estimated protein copy numbers of Arginase 2  
853 (ARG2; left) and alanine aminotransferase (GPT; right) for WT LN TCR $\beta$  CD8 $\alpha\beta$  and all 3 subsets of T-IEL.  
854 **(e)** Bar plots showing the estimated protein copy numbers of PRKR-Like Endoplasmic Reticulum  
855 Kinase (PERK) for WT LN TCR $\beta$  CD8 $\alpha\beta$  and all 3 T-IEL subsets. **(f)** Bar plots showing the OP-Puromycin  
856 (OPP) incorporation (n= 3 biological replicates) in *ex vivo* WT LN TCR $\beta$  CD8 $\alpha\beta$  and T-IEL. As a negative  
857 control, OPP incorporation was inhibited by cycloheximide (CHX) pre-treatment. OPP incorporation was  
858 assessed by flow cytometry 15 min after administration. Bar graph represents the geometric MFI of the OPP-  
859 AlexaFluor 647 in each T cell subsets normalized to the geometric MFI of the CHX pre-treated T cells. p-  
860 values were calculated using ordinary one-way ANOVA with Dunnett's multiple comparisons. For all box  
861 plots, the bottom and top hinges represent the 1<sup>st</sup> and 3<sup>rd</sup> quartiles. The top whisker extends from the hinge  
862 to the largest value no further than  $1.5 \times \text{IQR}$  from the hinge; the bottom whisker extends from the hinge to  
863 the smallest value at most  $1.5 \times \text{IQR}$  of the hinge. All bar plots show the mean and SEM. Symbols on the  
864 bars represent the biological replicates. The proteomics data displayed on the plots include WT TCR $\alpha\beta$   
865 CD8 $\alpha\beta$  T cells (n=6 biological replicates), TCR $\alpha\beta$ <sup>+</sup> CD8 $\alpha\beta$ <sup>+</sup> T-IEL and TCR $\alpha\beta$ <sup>+</sup> CD8 $\alpha\alpha$ <sup>+</sup> T-IEL (n=3 biological  
866 replicates) and TCR $\gamma\delta$ <sup>+</sup> CD8 $\alpha\alpha$ <sup>+</sup> T-IEL (n= 4 biological replicates). The P-values for individual proteins (c,d,e)  
867 were calculated in R with LIMMA, where \*\*= p < 0.001 and fold change greater than or equal to the median  
868 plus 1 standard deviation, \*\*\*= p < 0.0001 and fold change greater than or equal to the median +/- 1.5  
869 standard deviations, and in (a,b) in R with Welch's T test.

870 **Figure 3-source data 1: Sum of median copy numbers for the cytoplasmic and mitochondrial**  
871 **ribosomes**

872 **Figure 3- figure supplement 1: (a)** Box plots showing the median Log<sub>2</sub> fold change (T-IEL/LN CD8 T cells)  
873 for RNA Polymerase 1, 2 and 3 complexes. Each grey dot represents one of the polymerase subunits. P-  
874 values were calculated using one-sample t-tests, where \* = p < 0.05, \*\* = p < 0.01, \*\*\* = p < 0.001, ns = not  
875 significant. **(b)** Schematic representation of the urea cycle. Coloured heatmap squares represent protein  
876 expression Log<sub>2</sub> fold change (T-IEL/LN CD8 T cells) in, from left to right, T-IEL TCR $\beta$  CD8 $\alpha\beta$ , T-IEL TCR $\beta$   
877 CD8 $\alpha\alpha$  and T-IEL TCR $\gamma\delta$  CD8 $\alpha\alpha$ . Proteins expressed only by T-IEL are highlighted by red squares,  
878 representing estimated protein copy numbers (mean from at least 3 biological replicates). For protein names,  
879 see supplementary Table 4.

880 **Figure 4: Metabolic profiling of the T-IEL proteome**

881 **(a)** Stacked bar plots comparing the proportional representation of metabolic pathways in LN TCR $\beta$  CD8 $\alpha\beta$   
882 and all T-IEL subsets. **(b)** Bar plots showing the estimated protein copy numbers of the glucose transporters,

GLUT1, GLUT2 and GLUT3, for WT LN TCR $\beta$  CD8 $\alpha\beta$  and all 3 subsets of T-IEL. **(c)** Heatmaps displaying the Log<sub>2</sub> fold change (T-IEL/ LN CD8 T cells) for all proteins involved in glycolysis, tricarboxylic acid cycle (TCA cycle) and fatty acid oxidation (FAO). **(d)** Bar plots showing the sum of the estimated protein copy numbers of the electron transporter chain (ETC) components, for WT LN TCR $\beta$  CD8 $\alpha\beta$  and all 3 subsets of T-IEL. Sum of the copy numbers across all ETC complexes are available in Figure 4-source data 1. **(e)** Schematic representation of the glycerol 3-phosphate shuttle with heatmaps showing protein expression of cytosolic glycerol-3-phosphate dehydrogenase (cGpDH) and the Log<sub>2</sub> fold change of mitochondrial glycerol-3-phosphate dehydrogenase (mGpDH) (T-IEL/LN CD8 T cells) in, from left to right, T-IEL TCR $\beta$  CD8 $\alpha\beta$ , T-IEL TCR $\beta$  CD8 $\alpha\alpha$  and T-IEL TCR $\gamma\delta$  CD8 $\alpha\alpha$ . All bar plots show the mean and SEM. Symbols on the bars represent the biological replicates. The proteomics data displayed on the plots include WT TCR $\alpha\beta$  CD8 $\alpha\beta$  T cells (n=6 biological replicates), TCR $\alpha\beta$ <sup>+</sup> CD8 $\alpha\beta$ <sup>+</sup> T-IEL and TCR $\alpha\beta$ <sup>+</sup> CD8 $\alpha\alpha$ <sup>+</sup> T-IEL (n=3 biological replicates) and TCR $\gamma\delta$ <sup>+</sup> CD8 $\alpha\alpha$ <sup>+</sup> T-IEL (n= 4 biological replicates). P-values for individual proteins (b-c) were calculated in R with LIMMA, where \*\*= p <0.001 and fold change greater than or equal to the median plus 1 standard deviation, \*\*\*= p <0.0001 and fold change greater than or equal to the median +/- 1.5 standard deviations, and in (d) in R with Welch's T test. For full protein names, see Supplementary File 4.

**Figure 4-source data 1: Sum of median copy numbers for the all the ETC complexes**

**Figure 5: T-IEL have enhanced cholesterol and lipid metabolism**

**(a)** Schematic representation of proteins involved of the cholesterol biosynthetic pathway. Heatmap squares represent the Log<sub>2</sub> fold change (T-IEL/LN CD8 T cells) in, from left to right, T-IEL TCR $\beta$  CD8 $\alpha\beta$ , T-IEL TCR $\beta$  CD8 $\alpha\alpha$  and T-IEL TCR $\gamma\delta$  CD8 $\alpha\alpha$ . Proteins expressed only by T-IEL are highlighted by red squares, representing the mean estimated protein copy numbers (from at least 3 biological replicates). **(b)** Bar plot showing the estimated protein copy number of SREBP2 for WT LN TCR $\beta$  CD8 $\alpha\beta$  and all 3 subsets of T-IEL. **(c)** Bar plot showing a comparison of total cellular cholesterol content in sorted WT LN TCR $\beta$  CD8 $\alpha\beta$  and all 3 subsets of T-IEL (n=4 biological replicates). P-values calculated using ordinary one-way ANOVA with Dunnett's multiple comparison test. Data for the total cholesterol content are available in Figure 5-source data 1. **(d)** Bar plots showing the estimated protein copy numbers of the fatty acid transporters FATP1, FATP2 and FATP4 for WT LN TCR $\beta$  CD8 $\alpha\beta$  and all 3 subsets of T-IEL. **(e)** Bar plots showing the estimated protein copy numbers of the fatty acid binding proteins FABP1, FABP2, FABP5 and FABP6 for WT LN TCR $\beta$  CD8 $\alpha\beta$  and all 3 subsets of T-IEL. **(f)** Schematic representation of the triacylglycerol synthesis pathways and lipoprotein assembly. Coloured squares represent the Log<sub>2</sub> fold change (T-IEL/LN CD8 T cells) in, from left to right, T-IEL TCR $\beta$  CD8 $\alpha\beta$ , T-IEL TCR $\beta$  CD8 $\alpha\alpha$  and T-IEL TCR $\gamma\delta$  CD8 $\alpha\alpha$ . Proteins expressed only by T-IEL are highlighted by red squares, representing estimated protein copy numbers (mean from at least 3 biological replicates). All bar plots show the mean and SEM. Symbols on the bars represent the biological replicates. The proteomics data displayed on the plots include WT TCR $\alpha\beta$  CD8 $\alpha\beta$  T cells (n=6 biological replicates), TCR $\alpha\beta$ <sup>+</sup> CD8 $\alpha\beta$ <sup>+</sup> T-IEL and TCR $\alpha\beta$ <sup>+</sup> CD8 $\alpha\alpha$ <sup>+</sup> T-IEL (n=3 biological replicates) and TCR $\gamma\delta$ <sup>+</sup> CD8 $\alpha\alpha$ <sup>+</sup> T-IEL (n= 4 biological replicates). P-values for individual proteins (a,b,d,e,f) were calculated in R with LIMMA, where \*\*= p <0.001 and fold change greater than or equal to the median plus 1 standard deviation, \*\*\*= p <0.0001



922 and fold change greater than or equal to the median +/- 1.5 standard deviations. For full protein names, see  
923 Supplementary File 4.

924 **Figure 5-source data 1: Total cholesterol content across all populations**

925

926 **Figure 6: Cell surface proteins expressed on T-IEL**

927 **(a)** Schematic representation of proteins involved in cell-cell adhesion that are only expressed by the  
928 different T-IEL subsets. **(b)** Heatmaps displaying the estimated protein copy numbers of adhesion molecules,  
929 co-signalling receptors, neuropeptide receptors and purinergic receptors expressed only by T-IEL. Data  
930 represent the mean of at least 3 biological replicates. **(c)** Purified LN CD8 T cells (left) and isolated T-IEL  
931 (right) were immunostained for ZO-2 (top, red), E-cadherin (bottom, green) and CD8 $\alpha$  (not shown) and  
932 counterstained with DAPI to mark the nuclei (blue). Representative (of 2 independent experiments) maximal  
933 intensity projections of confocal sections spanning the entire cell thickness of selected CD8+ cells of each  
934 type are shown. Size bars = 2  $\mu$ m. See also Supplementary Figure 3. **(d)** Heatmap displaying Log<sub>2</sub> fold  
935 change (T-IEL/ LN CD8 T) cells of adhesion molecules, co-signalling receptors and purinergic receptors. The  
936 proteomics data displayed on the plots show the mean values and were calculated from WT TCR $\alpha\beta$  CD8 $\alpha\beta$   
937 T cells (n=6 biological replicates), TCR $\alpha\beta$ <sup>+</sup> CD8 $\alpha\beta$ <sup>+</sup> T-IEL and TCR $\alpha\beta$ <sup>+</sup> CD8 $\alpha\alpha$ <sup>+</sup> T-IEL (n=3 biological  
938 replicates) and TCR $\gamma\delta$ <sup>+</sup> CD8 $\alpha\alpha$ <sup>+</sup> T-IEL (n= 4 biological replicates). P-values were calculated in R with  
939 LIMMA, where \*\*= p <0.001 and fold change greater than or equal to the median plus 1 standard deviation,  
940 \*\*\*= p <0.0001 and fold change greater than or equal to the median +/- 1.5 standard deviations.

941

942 **Figure 6- figure supplement 1: Expression of epithelial proteins in T-IEL. a)** Bar plots showing the  
943 ImmGen microarray database ([www.immgen.org](http://www.immgen.org)) derived normalised RMA values for *Tjp2* (ZO2), *EpCam*  
944 and *Cdh1* (E-Cadherin) across WT naïve CD8 T cells (T.8Nve.Sp and T.8Nve.LN) and TCR $\gamma\delta$  V $\gamma$ 5-ve or  
945 V $\gamma$ 5+ve IEL (Tg.dVg5-.IEL, TgdVg5+IEL) **(b-c)** Comparison, by flow cytometry of the expression of EpCam  
946 **(b)** and E-Cadherin **(c)** in WT LN CD8 T cells, all 3 subsets of T-IEL and intestinal epithelial cells (IEC). Bar  
947 plots presenting geometric mean fluorescence intensities of n=3 biological replicates are shown on the side  
948 of each histogram. Mean  $\pm$  SEM shown. p-values were calculated using one-way ANOVA and Dunnett's  
949 multiple comparisons test. **(d)** Gating strategy used to identify T-IEL and IEC for (b-c). Lymphocytes and IEC  
950 were gated by size using forward scatter (FCS) and side scatter (SSC) and doublets were excluded. T-IEL  
951 subsets were separated as described in the FACS sorting strategy in supplementary Figure 1. **(e)** ZO-2 and  
952 E-cadherin immunofluorescence of IEL and WT LN CD8 T cells. Isolated IEL depleted of Annexin V-positive  
953 contaminants (IEL, top) and isolated purified LN CD8 T cells (LN, bottom) were fixed, permeabilised,  
954 immunostained for ZO-2 (green on overlay, left panels), E-cadherin (red on overlay, left panels) and CD8 $\alpha$   
955 (not shown) or with secondary antibodies only (right panels), and counterstained with DAPI to mark the  
956 nuclei (blue). Representative maximal intensity projections of confocal sections spanning the entire cell  
957 thickness of CD8 $\alpha$ -positive cells of each type are shown. Black and white images show individual ZO-2  
958 (middle rows) or E-cadherin (bottom rows) staining or matching secondary antibody-only controls. All images  
959 were acquired and processed identically. Size bars are 2  $\mu$ m.

960

961 **Figure 7: T-IEL share similarities with exhausted T cells**

962 **(a)** Flow cytometry dot plots comparing the expression of purinergic receptors (CD38/CD73, top and  
963 P2X7R/CD39, bottom) in WT LN TCR $\beta$  CD8 $\alpha\beta$  and all 3 subsets of T-IEL. **(b)** Stacked doughnut plot  
964 showing the percentages of cells from LN CD8 T cells and T-IEL expressing the indicated purinergic  
965 receptors, quantified by flow cytometry (n=1 biological replicate). **(c)** Flow cytometric histograms comparing  
966 the protein expression of the exhaustion markers, CD244, LAG-3, CD160 and CD96 in all 3 subsets of T-  
967 IEL. **(d)** Stacked doughnut plot showing the percentage of cell from LN CD8 T cells and T-IEL expressing the  
968 indicated exhaustion markers quantified by flow cytometry (n= 4 biological replicates). **(e)** Bar plot showing  
969 the result of the T cells exhaustion overrepresentation analyses in LN TCR $\beta$  CD8 $\alpha\beta$  and in TCR $\beta$  CD8 $\alpha\beta$  T-  
970 IEL. **(f)** Venn diagrams showing the commonality of proteins upregulated (top) and downregulated (bottom)  
971 during exhaustion and in TCR $\beta$  CD8 $\alpha\beta$  T-IEL. **(g)** Heatmap displaying the Log<sub>2</sub> fold change (T-IEL/LN CD8 T  
972 cells) of transcription factors associated with exhaustion in T cells. **(h)** Bar plots showing the estimated  
973 protein copy number of TOX (left) and flow cytometry derived MFI for TOX (right) for WT LN TCR $\beta$  CD8 $\alpha\beta$   
974 and all 3 subsets of T-IEL. The proteomics data displayed on the plots include WT TCR $\alpha\beta$  CD8 $\alpha\beta$  T cells  
975 (n=6 biological replicates), TCR $\alpha\beta$ <sup>+</sup> CD8 $\alpha\beta$ <sup>+</sup> T-IEL and TCR $\alpha\beta$ <sup>+</sup> CD8 $\alpha\alpha$ <sup>+</sup> T-IEL (n=3 biological replicates) and  
976 TCR $\gamma\delta$ <sup>+</sup> CD8 $\alpha\alpha$ <sup>+</sup> T-IEL (n= 4 biological replicates). The flow cytometry was performed on 3 biological  
977 replicates, representative of 2 independent experiments. P-values for individual proteins (g-h) were  
978 calculated in R with LIMMA where \*\*= p <0.001 and fold change greater than or equal to the median plus 1  
979 standard deviation, \*\*\*= p <0.0001 and fold change greater than or equal to the median +/- 1.5 standard  
980 deviations, for the flow cytometry data (h) in GraphPad prism using one-way ANOVA with Dunnett's multiple  
981 comparisons test. For full protein names, see Supplementary File 4.

982 **Figure 7-source data 1: Flow cytometry-based percentage of cells expressing exhaustion markers**  
983 **and TOX MFI**

984

985 **Figure 8: Rewiring of the TCR signalosome in T-IEL**

986 **(a-b)** Responses of WT LN CD8 T cells and T-IEL to TCR stimulation. Bar plots show the percentage of cells  
987 positive for **(a)** phospho-ERK1/2 (T202/Y204) and **(b)** phospho-S6 (S235/236) before and after anti-CD3  
988 stimulation. The Src kinase inhibitor PP2 was added as a control to show that induction of ERK1/2 and S6  
989 phosphorylation was specific. N=3 biological replicates, p-values were calculated by two-way ANOVA with  
990 Dunnett's multiple comparisons test. Data are available in Figure 8-source data 1. **(c-d)** Schematic  
991 representation of the main TCR signalling pathways comparing the expression of selected proteins in T-IEL  
992 and LN naïve T cells. **(c)** TCR and LAT signalosome. **(d)** signalling pathways downstream TCR receptor. All  
993 heatmap squares represent the Log<sub>2</sub> fold change (T-IEL/LN CD8 T cells) in, from left to right, T-IEL TCR $\beta$   
994 CD8 $\alpha\beta$ , T-IEL TCR $\beta$  CD8 $\alpha\alpha$  and T-IEL TCR $\gamma\delta$  CD8 $\alpha\alpha$ . Proteins expressed only by T-IEL are highlighted by  
995 red squares, representing estimated protein copy numbers (mean from at least 3 biological replicates). The  
996 proteomics data displayed on the plots was calculated from WT TCR $\alpha\beta$  CD8 $\alpha\beta$  T cells (n=6 biological  
997 replicates), TCR $\alpha\beta$ <sup>+</sup> CD8 $\alpha\beta$ <sup>+</sup> T-IEL and TCR $\alpha\beta$ <sup>+</sup> CD8 $\alpha\alpha$ <sup>+</sup> T-IEL (n=3 biological replicates) and TCR $\gamma\delta$ <sup>+</sup>  
998 CD8 $\alpha\alpha$ <sup>+</sup> T-IEL (n= 4 biological replicates). P-values were calculated in R with LIMMA, where \*\*= p <0.001  
999 and fold change greater than or equal to the median plus 1 standard deviation, \*\*\*= p <0.0001 and fold

1000 change greater than or equal to the median +/- 1.5 standard deviations. For protein names, see  
1001 Supplementary File 4.

1002 **Figure 8-source data 1: Flow cytometry-based percentage of cells positive for Phospho ERK1/2 and**  
1003 **phospho S6**

1004

1005 **Supplementary File 1:** Estimated protein copy numbers and differential expression analysis derived from  
1006 the mass spectrometric proteomics data for the 3 T-IEL subsets and WT and P14 LN T cells.

1007 **Supplementary File 2:** PANTHER Gene Ontology enrichment analysis

1008 **Supplementary File 3:** DAVID functional annotation enrichment analysis

1009 **Supplementary File 4** (related to Figure 4-8): Abbreviations and full protein names of proteins mentioned in  
1010 the text and figures.

1011 **Supplementary File 5** (related to Figure 7e-f): Proteins expressed in induced T-IEL and found to be  
1012 overrepresented in exhausted T cells gene set, and proteins missing or downregulated in induced T-IEL,  
1013 found to be underrepresented in exhausted T cells gene set (Khan et al, 2019).

1014 **Supplementary File 6:** Set up of TMT labelling of samples for proteomics

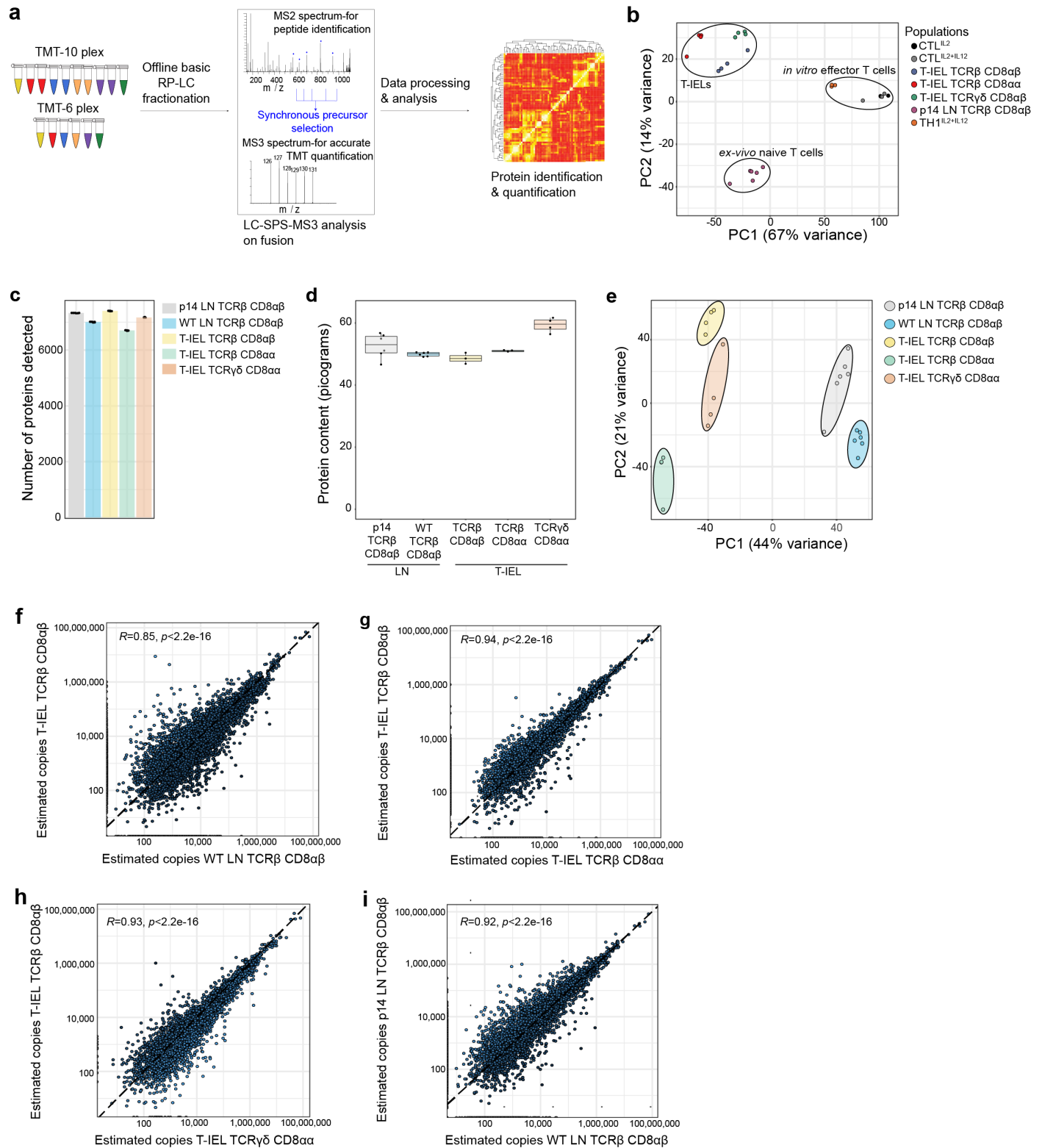
**Figure 1**

Figure 1- figure supplement 1

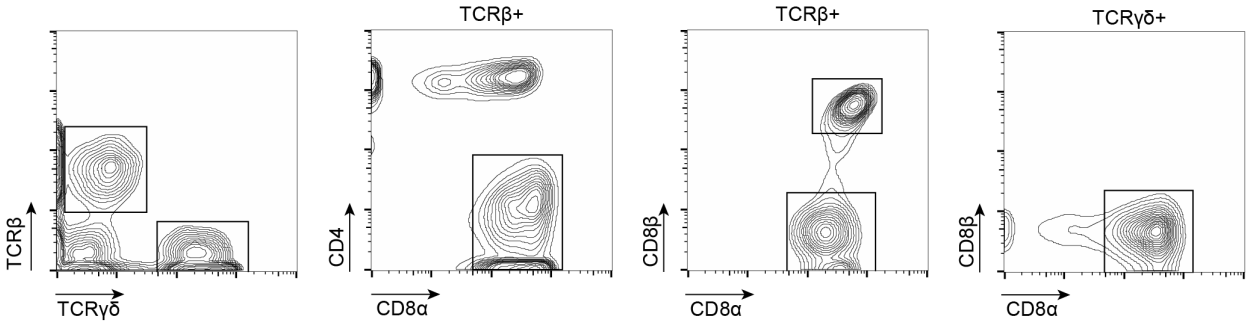
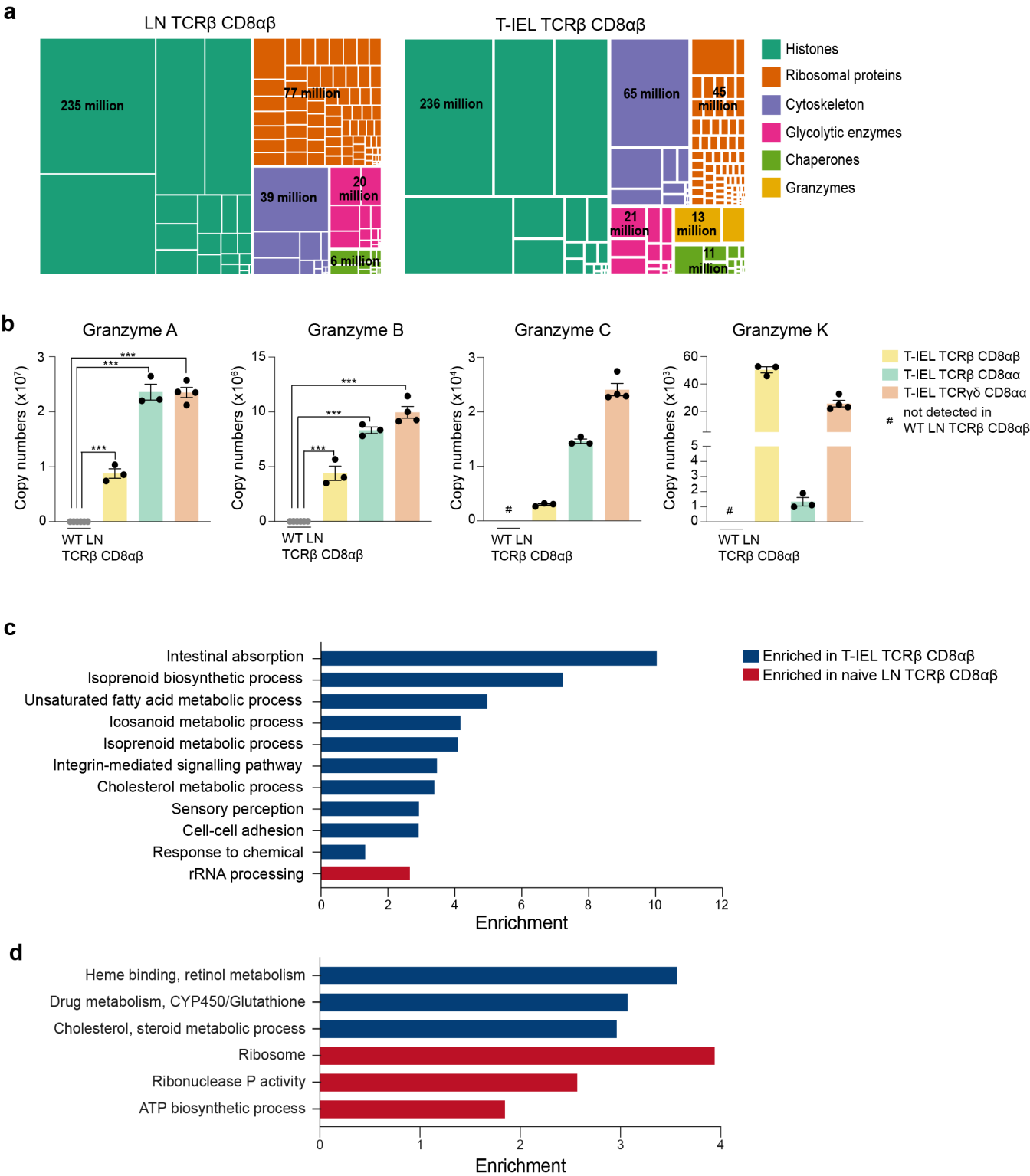


Figure 2



**Figure 3**

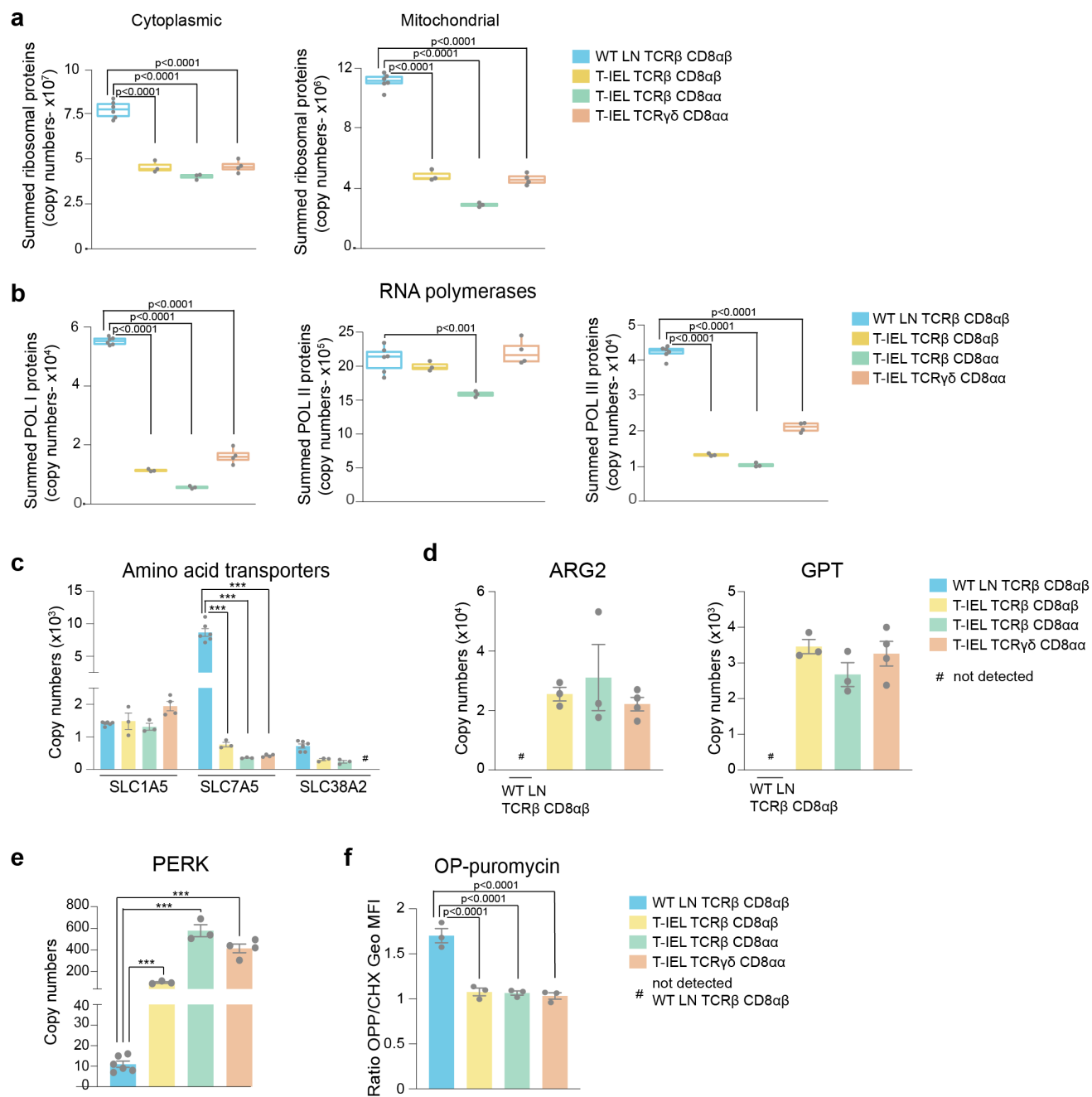
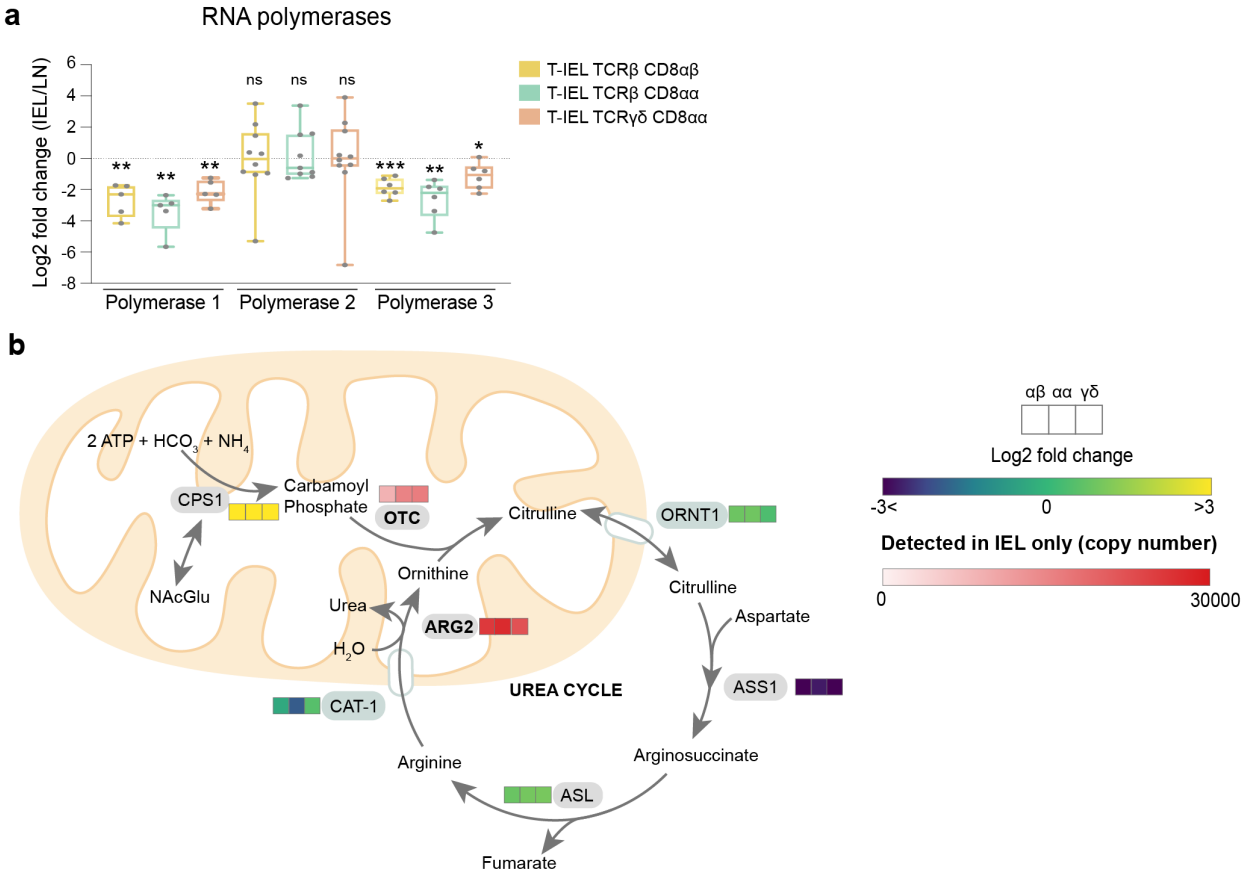
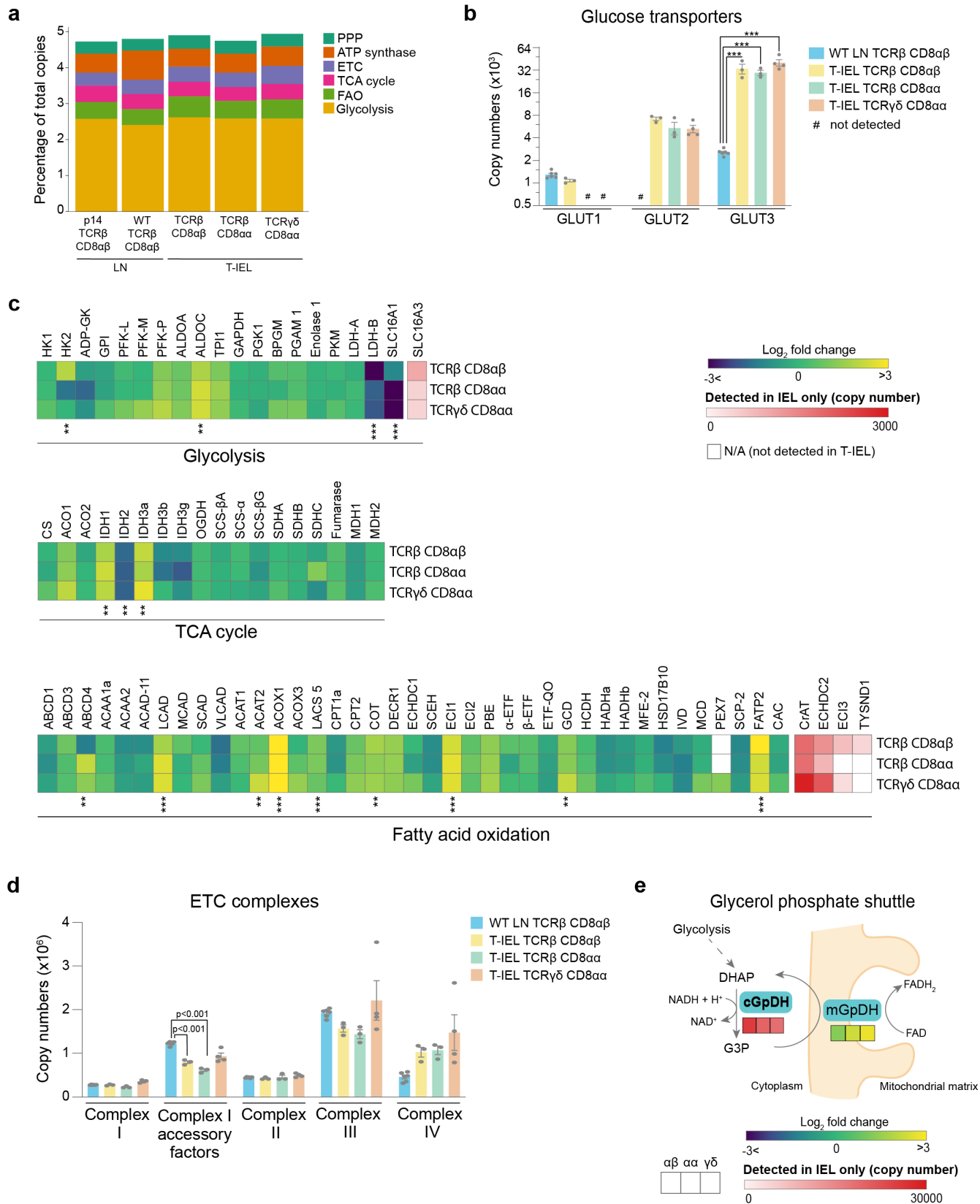


Figure 3-figure supplement 1





**Figure 4**



**Figure 5**

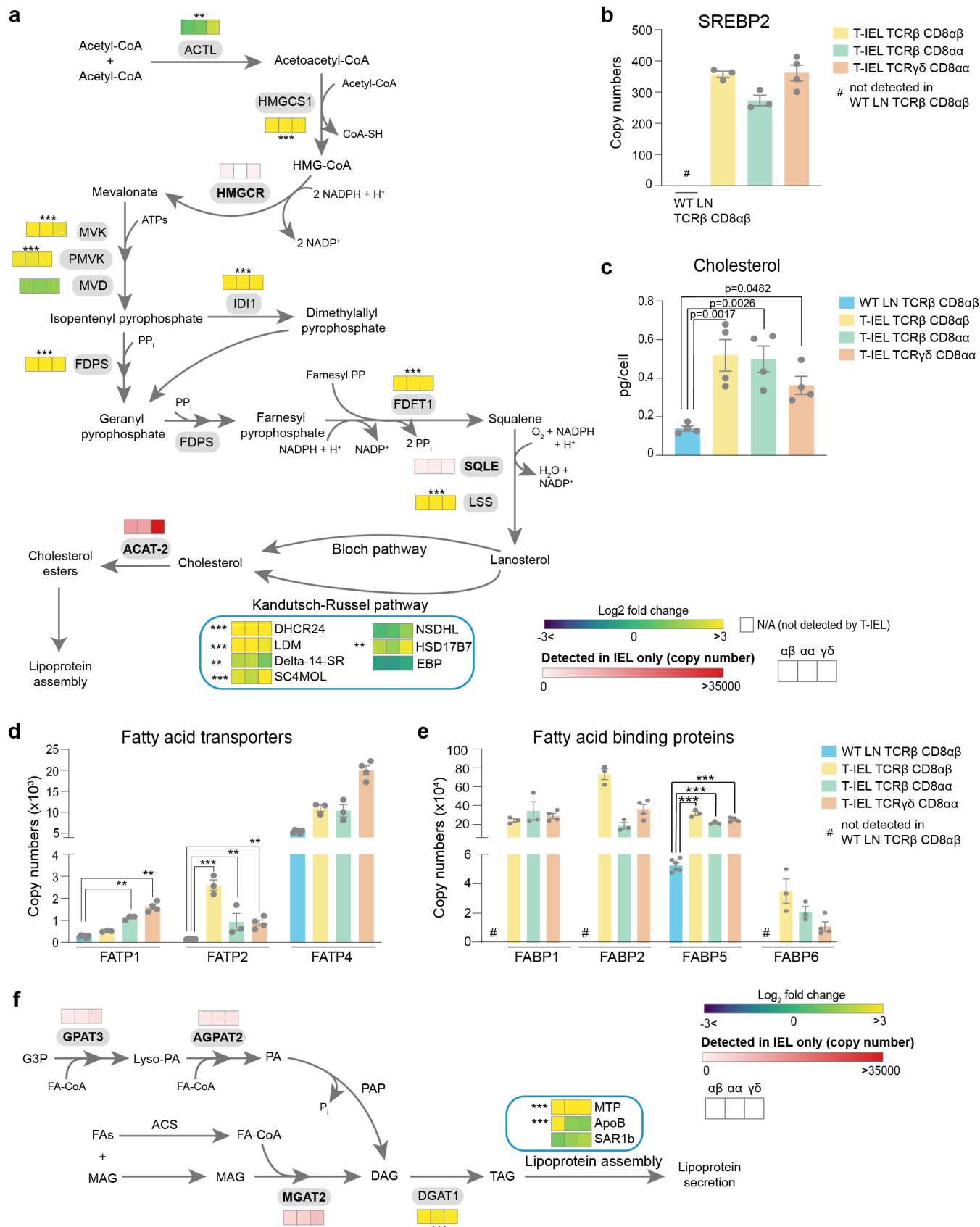


Figure 6

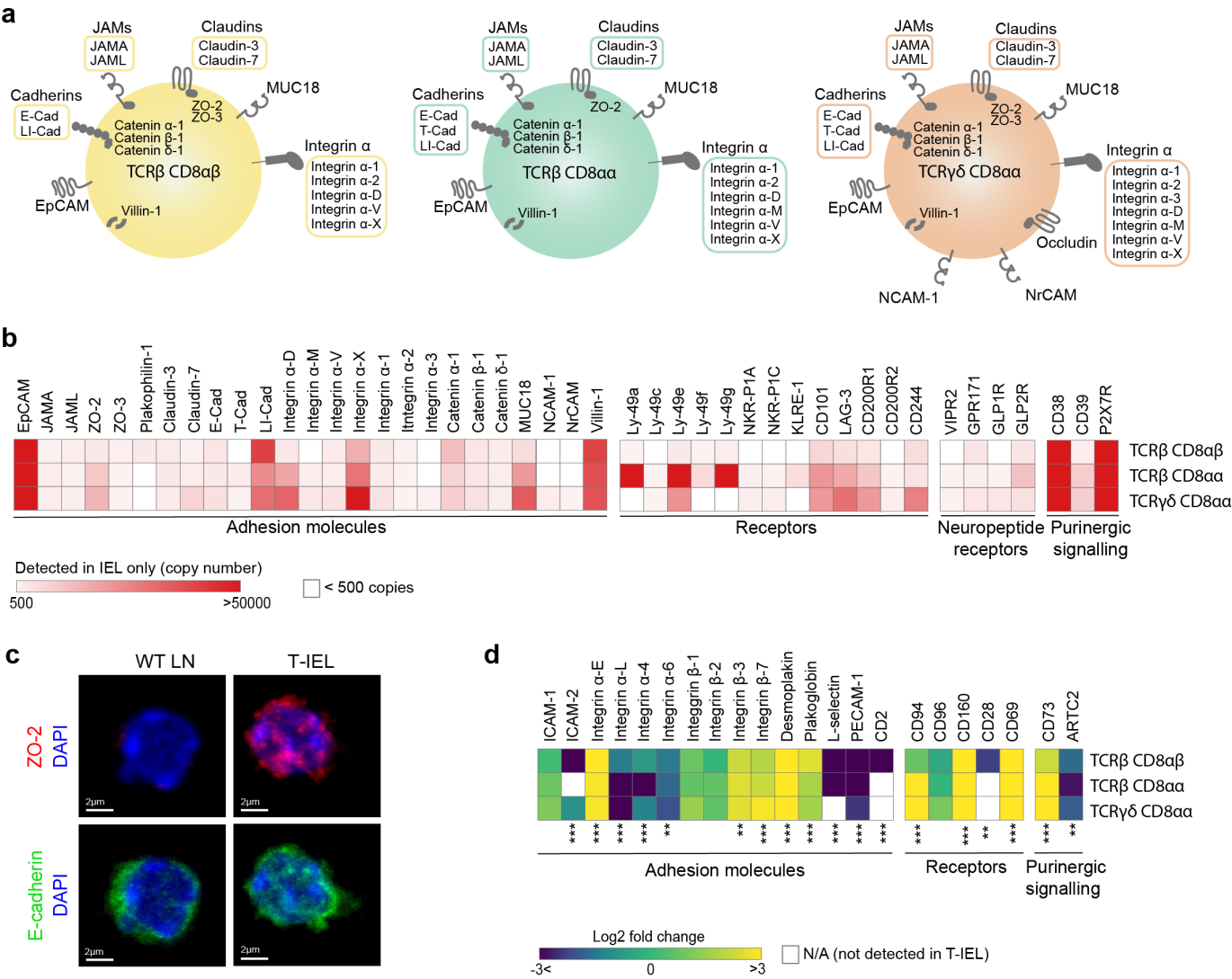


Figure 6- supplement figure 1

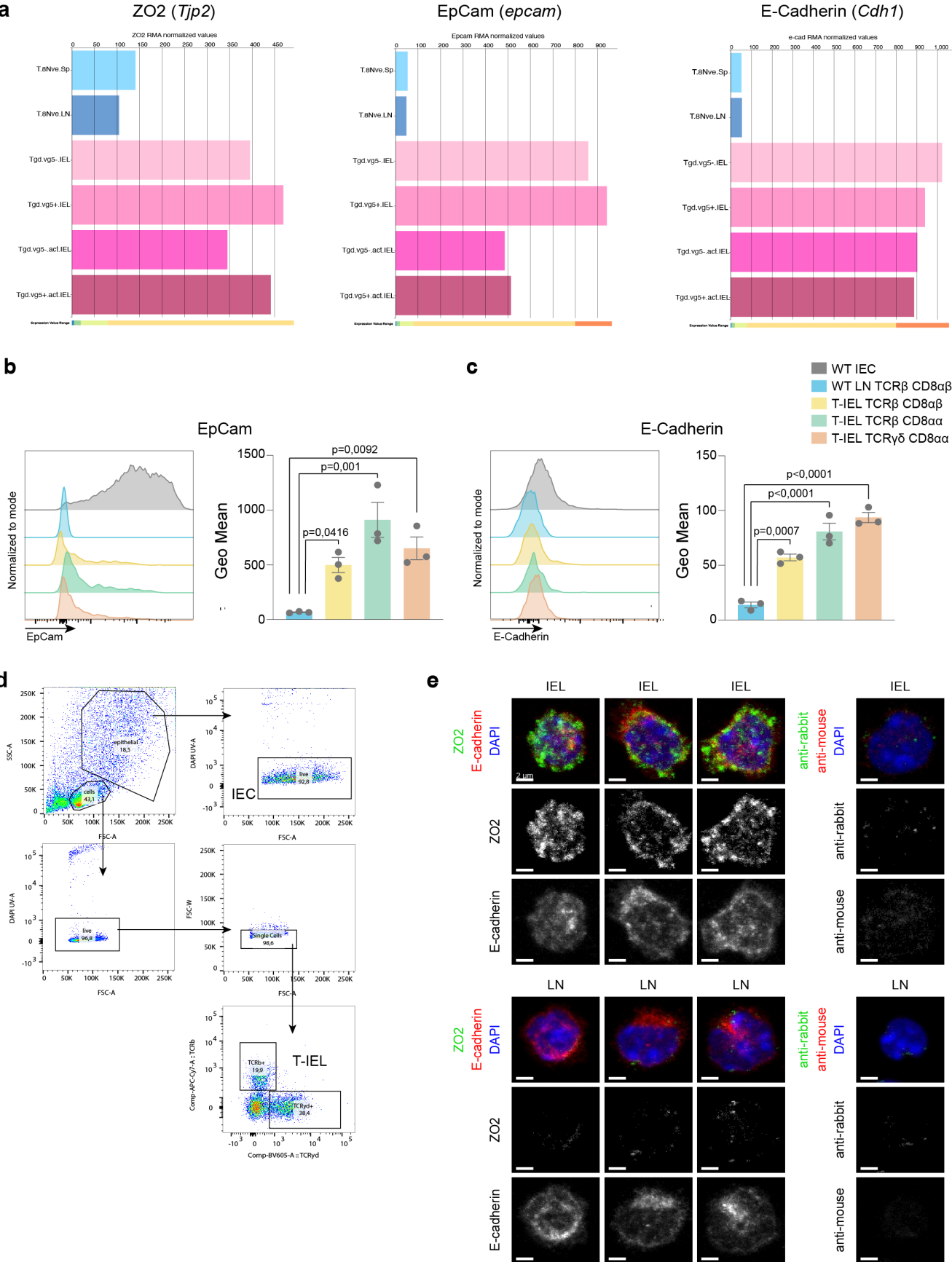
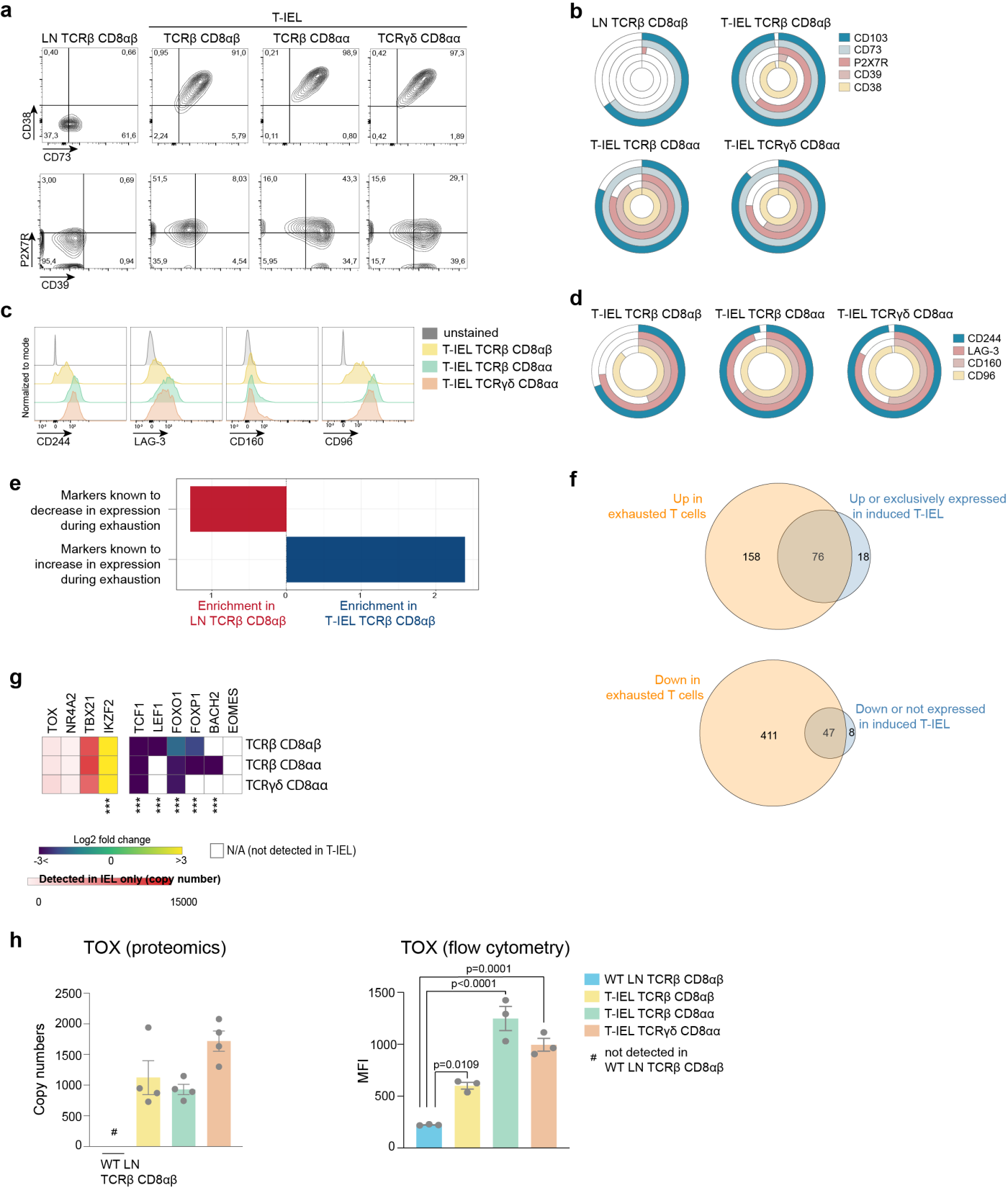


Figure 7



**Figure 8**

